The Journal of
Chemical Physics

Equation of state and force fields for Feynman–Hibbs-corrected Mie fluids. I. Application to pure helium, neon, hydrogen, and deuterium

Cite as: J. Chem. Phys. **151**, 064508 (2019); https://doi.org/10.1063/1.5111364
Submitted: 25 May 2019 . Accepted: 21 July 2019 . Published Online: 13 August 2019

Ailo Aasen, Morten Hammer, Åsmund Ervik, Erich A. Müller, and Øivind Wilhelmsen

J. Chem. Phys. **151**, 064508 (2019); https://doi.org/10.1063/1.5111364

The Journal of Chemical Physics ARTICLE scitation.org/journal/jcp

Equation of state and force fields for Feynman–Hibbs-corrected Mie fluids. I. Application to pure helium, neon, hydrogen, and deuterium

Cite as: J. Chem. Phys. **151**, 064508 (2019); doi: 10.1063/1.5111364
Submitted: 25 May 2019 • Accepted: 21 July 2019 •
Published Online: 13 August 2019

Ailo Aasen,[1,2,3,a)] **Morten Hammer,**[2,3] **Åsmund Ervik,**[2] **Erich A. Müller,**[3] **and Øivind Wilhelmsen**[1,2,3]

AFFILIATIONS

[1] Department of Energy and Process Engineering, Norwegian University of Science and Technology, NO-7491 Trondheim, Norway
[2] SINTEF Energy Research, NO-7465 Trondheim, Norway
[3] Department of Chemical Engineering, Imperial College London, London SW7 2AZ, United Kingdom

[a)] **Electronic mail:** ailo.aasen@ntnu.no

ABSTRACT

We present a perturbation theory that combines the use of a third-order Barker–Henderson expansion of the Helmholtz energy with Mie-potentials that include first- (Mie-FH1) and second-order (Mie-FH2) Feynman–Hibbs quantum corrections. The resulting equation of state, the statistical associating fluid theory for Mie potentials of variable range corrected for quantum effects (SAFT-VRQ-Mie), is compared to molecular simulations and is seen to reproduce the thermodynamic properties of generic Mie-FH1 and Mie-FH2 fluids accurately. SAFT-VRQ Mie is exploited to obtain optimal parameters for the intermolecular potentials of neon, helium, deuterium, *ortho*-, *para*-, and *normal*-hydrogen for the Mie-FH1 and Mie-FH2 formulations. For helium, hydrogen, and deuterium, the use of either the first- or second-order corrections yields significantly higher accuracy in the representation of supercritical densities, heat capacities, and speed of sounds when compared to classical Mie fluids, although the Mie-FH2 is slightly more accurate than Mie-FH1 for supercritical properties. The Mie-FH1 potential is recommended for most of the fluids since it yields a more accurate representation of the pure-component phase equilibria and extrapolates better to low temperatures. Notwithstanding, for helium, where the quantum effects are largest, we find that none of the potentials give an accurate representation of the entire phase envelope, and its thermodynamic properties are represented accurately only at temperatures above 20 K. Overall, supercritical heat capacities are well represented, with some deviations from experiments seen in the liquid phase region for helium and hydrogen.

I. INTRODUCTION

For most substances of practical interest, the thermodynamic properties of the fluid phase can be deduced from a classical statistical mechanical point of view, either through the development of analytical expressions (e.g., perturbation approaches) or through direct molecular simulations of a representative intermolecular potential. Under certain conditions, however, the classical approximations invoked break down and quantum effects start to become important. A typical gauge of the importance of quantum effects is the relative ratio of the de Broglie wavelength, $\lambda_B = h/\sqrt{2\pi m k_B T}$, to the typical length scale across which particles interact. Here, h and k_B are Planck's and Boltzmann's constants, m is the particle mass, and T is the temperature. Consequently, nonclassical effects should be strongest when particles have low mass, when temperatures are low, and when densities are high.

While, in principle, one could obtain the relevant average macroscopic properties through the solution of the Schrödinger equation, this is currently computationally infeasible for systems consisting of a large number of particles. Approximate treatments are therefore needed. Much effort was dedicated to this in the 1950s and 1960s, and significant progress was made then. The

Wigner–Kirkwood theory[1,2] was the first to describe quantum corrections to classical interaction potentials, and this theory was elegantly rederived and expanded upon by Feynman and Hibbs[3] using the path-integral formulation of quantum mechanics. Its key idea is that classical statistical mechanics can still be used to describe particles experiencing quantum effects, in as much as they are taken to interact through effective, temperature-dependent potentials. In 1969, Kim *et al.*[4] presented the first theoretical predictions of the quantum-corrected Lennard-Jones (LJ) potential using perturbation theory. However, after a flurry of research, the discussions on quantum corrections to the classical descriptions of fluids were left to the confines of key textbooks.[5–7] The start of the century brought renewed interest in the topic through the recognition that molecular simulations employing these *semiclassical* potentials could be used to study fluids such as helium, hydrogen, and neon at low temperatures by the use of classical molecular dynamics (MD) or Monte Carlo (MC) simulations. This simulation approach has since been used to study phenomena such as adsorption of hydrogen in porous materials,[8,9] quantum clusters,[10,11] helium at low temperatures,[12] and quantum fluids under confinement.[13]

Accurate thermodynamic property predictions of fluids with quantum effects are needed in a range of applications, for example to develop better hydrogen liquefaction processes.[14] At present, the most accurate representation of the thermodynamic properties of pure helium, neon, hydrogen, and deuterium is given by multiparameter Equations of State (EoSs).[15] For some fluids, multiparameter EoSs are capable of representing the available experimental data within their accuracy. However, these EoSs have challenges[16] that restrict their widespread application. A shortcoming of the multiparameter EoS framework is the lack of binary mixing models for helium, neon, hydrogen, and deuterium. Perturbation theory and SAFT (statistical associating fluid theory)-type of EoS, on the other hand, are readily extended to mixtures.[17,18] Another advantage of EoSs based on interaction potentials is that molecular simulations of the underlying force field can be leveraged to estimate transport properties such as viscosity, thermal conductivity, or interfacial properties such as the surface tension or the Kapitza resistance.[19] Furthermore, simulations can be used to obtain thermodynamic properties in regions outside of the domain of validity of the EoS.

A formally exact way to model the full quantum behavior is to use the Path Integral Monte Carlo approach,[20–23] but in practice the simpler semiclassical approach based on pair potentials is often preferred. Recently, Trejos and Gil-Villegas[24] presented a semiclassical Equation of State (EoS) valid for quantum fluids based on the statistical associating fluid theory for potentials of variable range (SAFT-VR), which they applied to the square well potential with a first-order quantum correction developed specifically for discontinuous potentials.[25,26] Contreras *et al.*[27] mapped the description of the quantum-corrected Lennard-Jones potential onto effective Mie potentials by building on the accurate third order perturbation theory that has been developed for Mie fluids.[18,28,29] While these approaches are all based on perturbation theory using hard spheres as references, there are also investigations on perturbations from quantum hard spheres.[30] It is in this context we place our contribution, presenting an accurate perturbation approach that provides both an equation of state and a set of semiclassical force fields for fluids where quantum effects are relevant.

This paper is structured as follows: In Sec. II, we present a SAFT-VR-type equation of state for Mie potentials with first and second order Feynman–Hibbs quantum corrections (SAFT-VRQ Mie). By comparing the results from Monte Carlo simulations (Sec. III), we demonstrate in Sec. IV that the new EoS has a similar accuracy as present state-of-the-art for classical Mie fluids. Available experimental data are used in a fitting procedure described in Sec. III C to determine the optimal parameters for helium, neon, hydrogen, and deuterium to evaluate the accuracy of the description.

II. THEORY

In the following, we build on the work by Lafitte *et al.*[18] and extend the statistical associating fluid theory for variable range Mie potentials (SAFT-VR Mie) equation of state (EoS) to Mie potentials with Feynman–Hibbs-corrections. The Feynman–Hibbs corrections will be introduced in Sec. II A, before the complete description of the quantum corrected EoS (SAFT-VRQ Mie) for single-component fluids is presented in Sec. II B. Throughout this work, the lowercase letter u denotes a pair potential.

A. The influence of quantum effects on the interaction potential–semiclassical potentials

At low temperatures, fluids such as hydrogen and helium are not accurately represented by the classical-mechanical description. Feynman and Hibbs, in their seminal book[3] on the path integral formulation of quantum mechanics, derived the quantum-mechanical partition function for a system of particles interacting with a given classical interaction potential, u_{C} (subscript C refers to classical). The classical potential determines the fluid behavior at temperatures where quantum effects are negligible, while at lower temperatures, the classical concept of interaction potential loses its meaning since particles are delocalized due to the wave-particle duality. However, the approximation known as the *effective potential method*[3] incorporates quantum effects but retains the concept of interaction potential. In this approximation, particles interact through an effective potential obtained by adding temperature- and mass-dependent corrections to the classical potential. Feynman and Hibbs[3] showed that an effective potential that approximately accounts for quantum effects is

$$u_{\mathrm{GFH}}(\boldsymbol{r}) = \left(\frac{6\mu}{\pi\beta\hbar^2}\right)^{3/2} \int_{\mathbb{R}^3} u_{\mathrm{C}}(\boldsymbol{r}+\boldsymbol{s}) \exp\left(\frac{-6\mu}{\beta\hbar^2}|\boldsymbol{s}|^2\right) \mathrm{d}\boldsymbol{s}, \qquad (1)$$

where $\boldsymbol{r}$ is the separation vector between two particles, $\mu = (m_1^{-1} + m_2^{-1})^{-1}$ is their reduced mass, $\beta = 1/k_{\mathrm{B}}T$ is the reduced inverse temperature, and $\hbar = h/2\pi$ is the reduced Planck's constant. Known as the Gaussian Feynman–Hibbs potential, this effective potential accounts for delocalization by taking a Gaussian average of the classical potential, where the width of the Gaussian equals the thermal de Broglie wavelength.

The more commonly used Feynman–Hibbs (FH) corrections can be obtained by a Taylor expansion of the potential in Eq. (1), yielding

$$u_{\mathrm{FHM}}(\boldsymbol{r}) = \sum_{n=0}^{\mathrm{M}} \frac{D^n}{n!} \nabla^{2n} u_{\mathrm{C}}(\boldsymbol{r}), \qquad D = \frac{\beta\hbar^2}{24\mu}. \qquad (2)$$

Here, M is the order of the Feynman–Hibbs correction. For most classical potentials, u_C, the series in Eq. (2) diverges pointwise everywhere in the limit $M \to \infty$ and must be interpreted as an asymptotic series.[31] Alternative derivations for the first- and second-order corrections, corresponding to $M = 1, 2$ in Eq. (2), exist.[3]

To represent classical potentials, we will use the Mie family of potentials,

$$u_C(r) = u_{\text{Mie}}(r) = \mathcal{C}\epsilon\left[\left(\frac{\sigma}{r}\right)^{\lambda_r} - \left(\frac{\sigma}{r}\right)^{\lambda_a}\right], \tag{3}$$

where ϵ is the well-depth, σ is the characteristic length scale corresponding to the distance at which the interparticle potential is zero, λ_a and λ_r are the attractive and repulsive exponents, and

$$\mathcal{C} = \left(\frac{\lambda_r}{\lambda_r - \lambda_a}\right)\left(\frac{\lambda_r}{\lambda_a}\right)^{\frac{\lambda_a}{\lambda_r - \lambda_a}}. \tag{4}$$

We will only consider effective potentials corresponding to the zeroth, first, and second order Feynman–Hibbs corrections to the classical Mie potential; these effective potentials will be referred to as Mie-FH0, Mie-FH1, and Mie-FH2, respectively. Theory and simulation studies based on these effective potentials have established them as successful in accounting for quantum corrections.[8,10,11,13,32,33] The complete expression for the quantum-corrected Mie-FH2 potential between particles of type i and j is

$$\begin{aligned} u(r)/(\mathcal{C}(\lambda_r,\lambda_a)\epsilon) = {} & \frac{\sigma^{\lambda_r}}{r^{\lambda_r}} - \frac{\sigma^{\lambda_a}}{r^{\lambda_a}} \\ & + D\left(Q_1(\lambda_r)\frac{\sigma^{\lambda_r}}{r^{\lambda_r+2}} - Q_1(\lambda_a)\frac{\sigma^{\lambda_a}}{r^{\lambda_a+2}}\right) \\ & + D^2\left(Q_2(\lambda_r)\frac{\sigma^{\lambda_r}}{r^{\lambda_r+4}} - Q_2(\lambda_a)\frac{\sigma^{\lambda_a}}{r^{\lambda_a+4}}\right), \end{aligned} \tag{5}$$

where

$$Q_1(\lambda) = \lambda(\lambda - 1), \tag{6}$$

$$Q_2(\lambda) = \frac{1}{2}(\lambda + 2)(\lambda + 1)\lambda(\lambda - 1), \tag{7}$$

$$D = \frac{\beta\hbar^2}{12m}. \tag{8}$$

The expressions for the Mie-FH1 potential are obtained by omitting the term in Eq. (5) with prefactor D^2. As illustrated in Fig. 1, the Feynman–Hibbs corrections influence pair potential in three different ways:

1. The effective particle diameter increases.
2. The effective potential well-depth decreases.
3. The range of the potential increases.

These effects become more pronounced as the temperature decreases, at a rate conveniently quantified by the de Boer parameter,

$$\Lambda = \frac{h}{\sigma\sqrt{m\epsilon}}. \tag{9}$$

One can interpret the de Boer parameter as the ratio between the de Broglie wavelength and a length which characterizes the intermolecular interactions. For fluids influenced by quantum effects, this dimensionless parameter is an additional parameter that must be used on top of the characteristic length and energy scales in any theory of corresponding states for quantum fluids.[7] Using the Lennard-Jones classical potential, Λ has been found to vary between approximately 0 (xenon) and approximately 3 (helium),[34] where higher values of Λ imply that quantum effects become more significant.

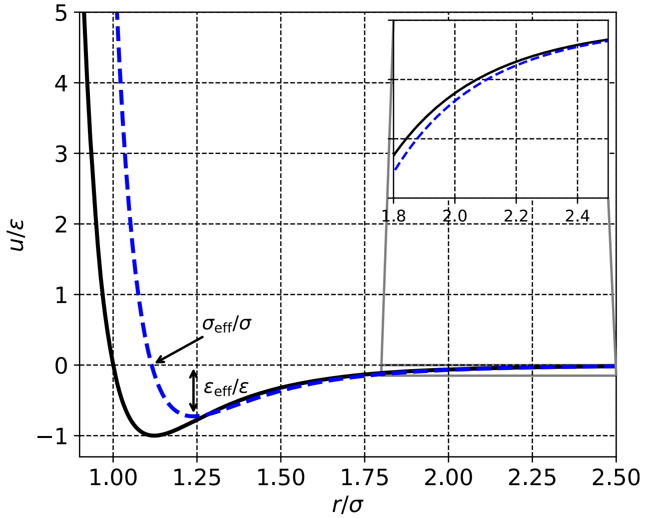

FIG. 1. Pair interaction potential for the LJ (black solid line) and LJ-FH2 (blue dashed line) potentials, at reduced temperature $T^* = 4$ and de Boer parameter $\Lambda = 3$. The FH correction increases the effective diameter σ_{eff} and decreases the well depth ϵ_{eff}, compared to the classical LJ parameters σ and ϵ. The inset in the upper right corner details how the effective range of the potential increases.

Exchange effects arise due to the indistinguishability of identical particles. At high temperatures, i.e., in the classical limit, exchange effects are approximated by including the factor $1/N!$ in the partition function; at low temperatures, this approximation is less accurate, especially for dense systems.[3] However, theoretical work[35,36] using $\hbar$-expansions indicates that the contribution to the effective potential from exchange effects is negligible. This work therefore ignores these effects.

B. The SAFT-VRQ Mie equation of state

The SAFT-VRQ Mie equation of state (where Q stands for quantum) is based on a third-order Barker–Henderson[7,37] perturbation theory and can be viewed as an extension of the monomer term of the SAFT-VR Mie EoS,[18,29] which is the present state-of-the-art perturbation theory for Mie fluids. The reduced, residual Helmholtz energy $a^{\text{res}} = A^{\text{res}}/Nk_BT$ can be written as

$$a^{\text{res}} = a^{\text{HS}} + \beta a_1 + \beta^2 a_2 + \beta^3 a_3, \tag{10}$$

where a^{HS} is the reduced, residual Helmholtz energy of a hard-sphere system of diameter d specified below, while a_1, a_2, and a_3 are the first-, second-, and third-order perturbation coefficients, respectively.

Following the perturbation theory of Barker and Henderson, we split the Mie-FH potential into a reference potential $u_0(r, \beta)$ and a perturbation potential $u_1(r,\beta)$, where

$$u_0(r,\beta) = \begin{cases} u_{\text{Mie-FH}}(r,\beta) & r \leq \sigma_{\text{eff}} \\ 0 & r > \sigma_{\text{eff}} \end{cases} \tag{11}$$

and

$$u_1(r,\beta) = \begin{cases} 0 & r \leq \sigma_{\text{eff}} \\ u_{\text{Mie-FH}}(r,\beta) & r > \sigma_{\text{eff}} \end{cases}, \tag{12}$$

where σ_{eff} is defined by the relation

$$u_{\text{Mie-FH}}(\sigma_{\text{eff}},\beta) = 0. \tag{13}$$

We emphasize that $\sigma_{\text{eff}}(T)$ is always larger than σ, except when there are no quantum corrections. The difference between σ and σ_{eff} is illustrated in Fig. 1.

1. The van der Waals attractive energy

Before addressing the terms in the perturbation theory, we define the van der Waals attractive energy of the fluid,

$$e^{\text{vdW}} = 2\pi \int_{\sigma_{\text{eff}}}^{\infty} u_{\text{Mie-FH}}(r,\beta) r^2 dr. \tag{14}$$

In the expressions for the second and third order terms in the perturbation theory, we will use the dimensionless van der Waals energy, α, defined by

$$\alpha = -\frac{e^{\text{vdW}}}{2\pi\epsilon_{\text{eff}}\sigma_{\text{eff}}^3}, \tag{15}$$

where ϵ_{eff} is defined as the minimum value of the effective potential,

$$\epsilon_{\text{eff}}(\beta) = \min_r \left(u_{\text{Mie-FH}}(r,\beta)\right). \tag{16}$$

This minimum is located at r_ϵ, which is found by solving

$$\frac{\partial u_{\text{Mie-FH}}(r_\epsilon,\beta)}{\partial r} = 0. \tag{17}$$

We emphasize that $\epsilon_{\text{eff}}(T) \neq \epsilon$, except when there are no quantum corrections. The difference between ϵ and ϵ_{eff} is illustrated in Fig. 1. For the quantum-corrected Mie potential, we split the dimensionless van der Waals energy, α, into contributions from the classical potential and the quantum corrections,

$$\alpha = \alpha^{\text{Mie}} + \alpha^{\text{FH1}} + \alpha^{\text{FH2}}, \tag{18}$$

$$\alpha^{\text{Mie}} = \frac{\mathcal{C}\epsilon}{\epsilon_{\text{eff}}}\left[\left(\frac{\sigma}{\sigma_{\text{eff}}}\right)^{\lambda_{\text{a}}}\frac{1}{\lambda_{\text{a}}-3} - \left(\frac{\sigma}{\sigma_{\text{eff}}}\right)^{\lambda_{\text{r}}}\frac{1}{\lambda_{\text{r}}-3}\right], \tag{19}$$

$$\alpha^{\text{FH1}} = \frac{\mathcal{C}\epsilon}{\epsilon_{\text{eff}}}\frac{D}{\sigma^2}\left[\left(\frac{\sigma}{\sigma_{\text{eff}}}\right)^{2+\lambda_{\text{a}}}\frac{Q_1(\lambda_{\text{a}})}{\lambda_{\text{a}}-1} - \left(\frac{\sigma}{\sigma_{\text{eff}}}\right)^{2+\lambda_{\text{r}}}\frac{Q_1(\lambda_{\text{r}})}{\lambda_{\text{r}}-1}\right], \tag{20}$$

$$\alpha^{\text{FH2}} = \frac{\mathcal{C}\epsilon}{\epsilon_{\text{eff}}}\left(\frac{D}{\sigma^2}\right)^2\left[\left(\frac{\sigma}{\sigma_{\text{eff}}}\right)^{4+\lambda_{\text{a}}}\frac{Q_2(\lambda_{\text{a}})}{\lambda_{\text{a}}+1} - \left(\frac{\sigma}{\sigma_{\text{eff}}}\right)^{4+\lambda_{\text{r}}}\frac{Q_2(\lambda_{\text{r}})}{\lambda_{\text{r}}+1}\right]. \tag{21}$$

2. The hard-sphere reference

Following Barker and Henderson,[37] we define the hard-sphere diameter d as

$$d = \int_0^{\sigma_{\text{eff}}} [1 - \exp(-\beta u_{\text{Mie-FH}}(r,\beta))] dr, \tag{22}$$

where the σ_{eff} is used as the upper integration limit. The Carnahan and Starling EoS[38] is used to describe the hard-sphere contribution, where the compressibility factor is given by

$$Z^{\text{HS}} = \frac{P^{\text{HS}}}{\rho k_{\text{B}} T} = \frac{1+\eta+\eta^2-\eta^3}{(1-\eta)^3}, \tag{23}$$

where P is the pressure, and the packing fraction, η, is calculated by using the number density $\rho = N/V$ and the hard-sphere diameter, d,

$$\eta = \frac{\rho\pi d^3}{6}. \tag{24}$$

The reduced isothermal compressibility of the hard-sphere EoS, given by Eq. (23), is

$$K^{\text{HS}} = k_{\text{B}} T \frac{\partial \rho}{\partial P^{\text{HS}}} = \frac{(1-\eta)^4}{1+4\eta+4\eta^2-4\eta^3+\eta^4}. \tag{25}$$

The reduced, residual Helmholtz energy of the hard-sphere system, a^{HS}, is found by integrating the residual part of the Carnahan and Starling EoS,

$$a^{\text{HS}} = \frac{1}{N k_{\text{B}} T}\int_V^{\infty}\left(P^{\text{HS}} - P^{\text{id}}\right) \mathrm{d}V = \frac{3-2\eta}{(1-\eta)^2}, \tag{26}$$

where $P^{\text{id}} = N k_{\text{B}} T/V$ is the ideal-gas pressure at the given temperature and volume. A statistical-mechanical argument[7] shows that the compressibility factor for the hard-sphere system is related to the value of the radial distribution function (RDF) at contact, $g_d^{\text{HS}}(d)$, by

$$Z^{\text{HS}} = 1 + 4\eta g_d^{\text{HS}}. \tag{27}$$

Using the Carnahan and Starling expression in Eq. (23) for Z^{HS}, the quantity $g_d^{\text{HS}}(d)$ can thus be written as

$$g_d^{\text{HS}}(d) = \frac{1-\eta/2}{(1-\eta)^3}. \tag{28}$$

3. The first-order perturbation term

The first order perturbation term is given by[39]

$$a_1 = 2\pi\rho \int_{\sigma_{\text{eff}}}^{\infty} g_d^{\text{HS}}(r) u_{\text{Mie-FH}}(r,\beta) r^2 dr, \tag{29}$$

where $g_d^{\text{HS}}(r)$ is the radial distribution function of the hard-sphere fluid at position r. Gil-Villegas *et al.*[28] found that they could accurately correlate a_1 using algebraic expressions, thus avoiding numerical evaluation of the integral with quadrature techniques. For the square-well potential fluid, the contact diameter equals σ, and the integration is from σ to ∞. For soft potentials however, Lafitte *et al.*[18] showed that it was necessary to split the integral of a_1 into two parts, since the radial distribution function (RDF) at contact is given at $d \neq \sigma$. The same approach is followed in this work. By first integrating from d to ∞, and then including a correction integral from d to σ, a_1 can be written as

$$a_1 = 2\pi\rho \int_d^\infty g_d^{\mathrm{HS}}(r) u_{\text{Mie-FH}}(r,\beta) r^2 dr \tag{30}$$

$$- 2\pi\rho \int_d^{\sigma_{\mathrm{eff}}} g_d^{\mathrm{HS}}(r) u_{\text{Mie-FH}}(r,\beta) r^2 dr \tag{31}$$

$$= I_{1\mathrm{A}} + I_{1\mathrm{B}}. \tag{32}$$

Similar to the classical Mie potentials, the $u_{\text{Mie-FH}}$ potentials can be represented as a sum of generalized Sutherland potentials, described by a power law in r,

$$u^{\mathrm{S}}(r;\lambda) = -\epsilon\left(\frac{\sigma}{r}\right)^\lambda. \tag{33}$$

The definition of the generalized Sutherland potential presented in Eq. (33) does not include the hard-core part. We introduce the following scaling factors for the different parts of the potential:

$$\tilde{Q}_0 = 1, \tag{34}$$

$$\tilde{Q}_1(\lambda) = Q_1(\lambda)\frac{D}{\sigma^2}, \tag{35}$$

$$\tilde{Q}_2(\lambda) = Q_2(\lambda)\left(\frac{D}{\sigma^2}\right)^2. \tag{36}$$

The Feynman–Hibbs-corrected Mie potential can then be written as

$$\begin{aligned} u_{\text{Mie-FH}}(r) = &-\tilde{Q}_0 u^{\mathrm{S}}(r;\lambda_{\mathrm{r}}) + \tilde{Q}_0 u^{\mathrm{S}}(r;\lambda_{\mathrm{a}}) \\ &- \tilde{Q}_1(\lambda_{\mathrm{r}}) u^{\mathrm{S}}(r;\lambda_{\mathrm{r}}+2) + \tilde{Q}_1(\lambda_{\mathrm{a}}) u^{\mathrm{S}}(r;\lambda_{\mathrm{a}}+2) \\ &- \tilde{Q}_2(\lambda_{\mathrm{r}}) u^{\mathrm{S}}(r;\lambda_{\mathrm{r}}+4) + \tilde{Q}_2(\lambda_{\mathrm{a}}) u^{\mathrm{S}}(r;\lambda_{\mathrm{a}}+4). \end{aligned} \tag{37}$$

The a_1 integration can therefore be performed as a sum of integrals over Sutherland potentials, $a_1^{\mathrm{S}}(\lambda)$. To simplify the integration, the reduced center–center distance, $x = r/d$, between two hard spheres of diameter d is introduced. Furthermore, it is convenient to define $x_0 = \sigma/d$ and $x_{\mathrm{eff}} = \sigma_{\mathrm{eff}}/d$. This gives the following result for the contributions to a_1:

$$\begin{aligned} a_1^{\mathrm{S}}(\lambda) &= 2\pi\rho \int_d^\infty g_d^{\mathrm{HS}}(r) u^{\mathrm{S}}(r;\lambda) r^2 dr \\ &= 2\pi\rho d^3 \int_1^\infty g_d^{\mathrm{HS}}(xd) u^{\mathrm{S}}(xd;\lambda) x^2 dx. \end{aligned} \tag{38}$$

The Mean-Value Theorem (MVT) states that[18]

$$\int_1^\infty g_d^{\mathrm{HS}}(xd) u^{\mathrm{S}}(xd;\lambda) x^2 dx = g_d^{\mathrm{HS}}(\xi) \int_1^\infty u^{\mathrm{S}}(xd;\lambda) x^2 dx \tag{39}$$

for some $\xi \in [d, \infty)$. The van der Waals attractive energy for the Sutherland potential can be integrated analytically to give

$$a_1^{\mathrm{S}}(\lambda) = -12\eta\epsilon x_0^\lambda \left(\frac{1}{\lambda-3}\right) g_d^{\mathrm{HS}}(\xi). \tag{40}$$

Gil-Villegas *et al.*[28] showed that $g_d^{\mathrm{HS}}(\xi;\eta)$ can be correlated by using an effective packing fraction η_{eff}, giving $g_d^{\mathrm{HS}}(\xi;\eta) = g_d^{\mathrm{HS}}(1;\eta_{\mathrm{eff}})$. Lafitte *et al.* developed this further for the Mie potential, and the same λ correlation for η_{eff} as presented in Refs. 18 and 40 has been used in this work. For completeness, we repeat the correlations here. First,

$$g_d^{\mathrm{HS}}(\eta;\lambda) \approx \frac{1 - \eta_{\mathrm{eff}}(\eta;\lambda)/2}{(1 - \eta_{\mathrm{eff}}(\eta;\lambda))^3}, \tag{41}$$

where the effective packing fraction correlation is given by

$$\eta_{\mathrm{eff}}(\eta;\lambda) = c_1(\lambda)\eta + c_2(\lambda)\eta^2 + c_3(\lambda)\eta^3 + c_4(\lambda)\eta^4, \tag{42}$$

and is valid for $5 < \lambda \leq 100$. The coefficients in Eq. (42) are given from

$$\begin{pmatrix} c_1 \\ c_2 \\ c_3 \\ c_4 \end{pmatrix} = \begin{pmatrix} 0.81096 & 1.7888 & -37.578 & 92.284 \\ 1.0205 & -19.341 & 151.26 & -463.50 \\ -1.9057 & 22.845 & -228.14 & 973.92 \\ 1.0885 & -6.1962 & 106.98 & -677.64 \end{pmatrix} \begin{pmatrix} 1 \\ 1/\lambda \\ 1/\lambda^2 \\ 1/\lambda^3 \end{pmatrix}. \tag{43}$$

The complete integral for $I_{1\mathrm{A}}$ is then approximated as a sum of contributions from Sutherland potentials,

$$I_{1\mathrm{A}} \approx \mathcal{C} \sum_j w_j a_1^{\mathrm{S}}(\eta;\lambda_j), \tag{44}$$

where w_j are the prefactors from Eq. (37): the prefactor becomes $\pm\tilde{Q}_0$ for the Mie potential, $-\tilde{Q}_1(\lambda_{\mathrm{r}})$ and $\tilde{Q}_1(\lambda_{\mathrm{a}})$ for the FH1 contribution, and $-\tilde{Q}_2(\lambda_{\mathrm{r}})$ and $\tilde{Q}_2(\lambda_{\mathrm{a}})$ for the FH2 contribution.

Nezbeda and Iglesias-Silva[41] successfully used a linearization of the RDF to approximate it in the vicinity of contact ($x = 1$). The RDF is then described from the RDF at contact and its differential,

$$g_d^{\mathrm{HS}}(xd) \approx g_d^{\mathrm{HS}}(d) + (x-1)\left(\frac{\partial g_d^{\mathrm{HS}}(xd)}{\partial x}\right)_{x=1}. \tag{45}$$

Using Wertheim[42] theory, they derived the following differential:

$$\left(\frac{\partial g_d^{\mathrm{HS}}(xd)}{\partial x}\right)_{x=1} = -\frac{9(1+\eta)}{(1-\eta)^3}. \tag{46}$$

By using this approximation, the second integral of Eq. (30) simplifies to

$$\begin{aligned} I_{1\mathrm{B}} \approx -12\eta\Bigg[& g_d^{\mathrm{HS}}(d) \int_1^{x_{\mathrm{eff}}} u_{\text{Mie-FH}}(xd,\beta) x^2 dx \\ &+ \left(\frac{\partial g_d^{\mathrm{HS}}(xd)}{\partial x}\right)_{x=1} \int_1^{x_{\mathrm{eff}}} u_{\text{Mie-FH}}(xd,\beta)(x-1) x^2 dx\Bigg]. \end{aligned} \tag{47}$$

Expressing the quantum-corrected Mie potential in the hard-sphere reduced center–center distance variable, x, gives terms of type $x^{-\lambda}$ inside the integrand. To simplify the integration further, the integral functions I_λ and J_λ are introduced,

$$I_\lambda(\lambda) = \int_1^{x_{\mathrm{eff}}} \frac{x^2}{x^\lambda} dx = -\frac{x_{\mathrm{eff}}^{(3-\lambda)} - 1}{\lambda - 3}, \tag{48}$$

$$J_\lambda(\lambda) = \int_1^{x_{\mathrm{eff}}} \frac{(x^3 - x^2)}{x^\lambda} dx \tag{49}$$

$$= -\frac{x_{\mathrm{eff}}^{(4-\lambda)}(\lambda-3) - x_{\mathrm{eff}}^{(3-\lambda)}(\lambda-4) - 1}{(\lambda-3)(\lambda-4)}. \tag{50}$$

The contribution from each term of the effective quantum potential to the integral I_{1B} can then be described using B and the prefactor w_j,

$$I_{1\mathrm{B}} \approx \mathcal{C} \sum_j w_j x_0^{\lambda_j} B(\eta;\lambda_j), \tag{51}$$

with

TABLE I. $\phi_{i,n}$ coefficients.

n	$\phi_{1,n}$	$\phi_{2,n}$	$\phi_{3,n}$	$\phi_{4,n}$	$\phi_{5,n}$	$\phi_{6,n}$	$\phi_{7,n}$
0	7.536 555 7	−359.44	1550.9	−1.199 32	−1911.28	9236.9	10
1	−37.604 63	1825.6	−5070.1	9.063 632	21 390.175	−129 430	10
2	71.745 953	−3168.0	6534.6	−17.948 2	−51 320.7	357 230	0.57
3	−46.835 52	1884.2	−3288.7	11.340 27	37 064.54	−315 530	−6.7
4	−2.467 982	−0.823 76	−2.7171	20.521 42	1103.742	1390.2	−8
5	−0.502 72	−3.193 5	2.0883	−56.637 7	−3264.61	−4518.2	. . .
6	8.095 688 3	3.709 0	0	40.536 83	2556.181	4241.6	. . .

$$B(\eta;\lambda) = 12\eta\epsilon\left(\frac{1-\eta/2}{(1-\eta)^3}I_\lambda(\lambda) - \frac{9\eta(1+\eta)}{2(1-\eta)^3}J_\lambda(\lambda)\right). \tag{52}$$

4. The second-order perturbation term

The second order perturbation is approximated by the following expression:[18]

$$a_2 = -\pi\rho K^{\mathrm{HS}}(1+\chi)\int_{\sigma_{\mathrm{eff}}}^{\infty} g_d^{\mathrm{HS}}(r)\left(u_{\text{Mie-FH}}(r,\beta)\right)^2 r^2\,dr, \tag{53}$$

where the isothermal compressibility of the hard-sphere reference K^{HS} is described by Eq. (25) and χ is a correlated correction factor.

Using Eq. (37), the quadratic potential term of the integral, $(u_{\text{Mie-FH}}(r,\beta))^2$, can be expressed as a new sum of Sutherland potentials. For the Mie potential, there are three terms corresponding to the first three terms of Eq. (54). The FH1 potential is represented with the first nine terms of Eq. (54), while for the FH2 potential there are 18 terms,

$$\begin{aligned} u^2_{\text{Mie-FH}} = {} & u^{\mathrm{S}}(r;2\lambda_a) + u^{\mathrm{S}}(r;2\lambda_r) - 2u^{\mathrm{S}}(r;\lambda_r+\lambda_a) + \tilde{Q}_{1a}u^{\mathrm{S}}(r;2\lambda_a+2) + \tilde{Q}_{1r}u^{\mathrm{S}}(r;2\lambda_r+2) - \left[\tilde{Q}_{1a}+\tilde{Q}_{1r}\right]u^{\mathrm{S}}(r;\lambda_a+\lambda_r+2) \\ & + \tilde{Q}_{1a}^2u^{\mathrm{S}}(r;2\lambda_a+4) + \tilde{Q}_{1r}^2u^{\mathrm{S}}(r;2\lambda_r+4) - 2\tilde{Q}_{1a}\tilde{Q}_{1r}u^{\mathrm{S}}(r;\lambda_a+\lambda_r+4) + \tilde{Q}_{2a}u^{\mathrm{S}}(r;2\lambda_a+4) + \tilde{Q}_{2r}u^{\mathrm{S}}(r;2\lambda_r+4) \\ & - (\tilde{Q}_{2a}+\tilde{Q}_{2r})u^{\mathrm{S}}(r;\lambda_a+\lambda_r+4) + \tilde{Q}_{2a}\tilde{Q}_{1a}u^{\mathrm{S}}(r;2\lambda_a+6) + \tilde{Q}_{2r}\tilde{Q}_{1r}u^{\mathrm{S}}(r;2\lambda_r+6) - (\tilde{Q}_{2a}\tilde{Q}_{1r}+\tilde{Q}_{2r}\tilde{Q}_{1a})u^{\mathrm{S}}(r;\lambda_a+\lambda_r+6) \\ & + \tilde{Q}_{2a}^2u^{\mathrm{S}}(r;2\lambda_a+8) + \tilde{Q}_{2r}^2u^{\mathrm{S}}(r;2\lambda_r+8) - 2\tilde{Q}_{2a}\tilde{Q}_{2r}u^{\mathrm{S}}(r;\lambda_a+\lambda_r+8). \end{aligned} \tag{54}$$

Here, $\tilde{Q}_{1a} = \tilde{Q}_1(\lambda_a)$, $\tilde{Q}_{1r} = \tilde{Q}_1(\lambda_r)$, and likewise for $\tilde{Q}_2$.

To represent the correction factor, χ, we have used the same correlation as Lafitte *et al.*,[18]

$$\chi = f_1(\alpha)\bar{\zeta}_x + f_2(\alpha)\bar{\zeta}_x^5 + f_3(\alpha)\bar{\zeta}_x^8, \tag{55}$$

but with a different definition of the dimensionless van der Waals parameter, α [see Eq. (18) and Sec. II B 1 for a discussion]. Here, $\bar{\zeta}_x$ is defined as

$$\bar{\zeta}_x = \frac{\pi\rho\sigma_{\mathrm{eff}}^3}{6}. \tag{56}$$

f_i are correlations of the dimensionless van der Waals energy, α, and is given by

$$f_i(\alpha) = \frac{\sum_{n=0}^{n=3}\phi_{i,n}\alpha^n}{1+\sum_{n=4}^{n=6}\phi_{i,n}\alpha^{n-3}}, \quad i \in 1,\ldots,6, \tag{57}$$

where the coefficients are given in Table I.

5. The third-order perturbation term

To represent the third order perturbation term, we have used the same correlation as developed by Lafitte *et al.*,[18] but with the effective well depth and the effective dimensionless van der Waals parameters as input,

$$a_3 = -\epsilon_{\mathrm{eff}}^3 f_4(\alpha)\bar{\zeta}_x \exp\left(f_5(\alpha)\bar{\zeta}_x + f_6(\alpha)\bar{\zeta}_x^2\right). \tag{58}$$

III. NUMERICAL METHODS

In this section, we provide details on numerical aspects related to solving the EoS in Sec. III A, how the Monte Carlo simulations have been set up in Sec. III B and how the parameter fitting procedure has been carried out in Sec. III C. The EoS was implemented in the in-house thermodynamic library presented in Ref. 16, and we refer to previous work for details on routines for solving phase equilibria.[43–46]

A. Details on the numerics in the solution of SAFT-VRQ Mie

1. Solving for the effective diameter and well-depth

When calculating properties from SAFT-VRQ Mie, additional complexities appear that are not present for classical Mie fluids.[18] While Mie potentials are explicit in σ and ϵ, the corresponding quantities for the quantum-corrected potential, σ_{eff} and ϵ_{eff}, are only defined implicitly and must be obtained by iterative procedures. Furthermore, since they are functions of β, these parameters must be determined at each temperature. We calculated σ_{eff} by solving $u_{\text{Mie-FH}}(r, \beta) = 0$ with a Newton-Raphson solver with analytical derivatives and using the value of σ from the Mie potential as initial guess. In a similar manner, the effective well depth, ϵ_{eff}, was determined by solving Eq. (17), $\partial u_{\text{Mie-FH}}(r, \beta)/\partial r = 0$, for $r_{\epsilon_{\text{eff}}}$ with analytical derivatives in the Newton-Raphson solver and the value of r_ϵ from the Mie potential as initial guess. The effective well depth was then determined from Eq. (16).

2. Integration of the hard-sphere diameter

The Barker and Henderson[37] hard-sphere diameter is defined by Eq. (22), where the integral must be evaluated numerically. Figure 2 shows how the integrand, I_d, varies with the distance between two particles for the LJ potential at two different temperatures. It illustrates that in the region enclosed by $r/\sigma = 0$ and the dashed vertical lines, the integrand is numerically indistinguishable from one, and thus effectively constant. To integrate numerically in the entire interval, [0, 1] is therefore inefficient, as a large number of points would be needed in a quadrature to obtain an accurate estimate of the hard-sphere diameter. In this work, we followed a different strategy by first determining the region where the integrand was effectively constant. The hard-sphere diameter integrand is given as

$$I_d = 1 - \exp(-\beta u_{\text{Mie-FH}}(r, \beta)). \tag{59}$$

To determine the maximum distance, r_d, where $I_d = 1$ for the numerical integration is equivalent to solving $\exp(-\beta u_{\text{Mie-FH}}(r, \beta)) = \varepsilon$, where ε is the machine precision for the floating point representation used in the integration. The distance where the integrand becomes numerically invariant in a double precision integration is illustrated by the vertical dashed lines in Fig. 2. To determine the vertical dashed lines typically requires 5 or 6 evaluations of the potential function and the first and second order differentials, where we used a second order Newton solver. After splitting the integration region into two parts, the integration in the region $[r_d, \sigma_{\text{eff}}]$ was carried out to a high accuracy by using a 21 point Gauss–Kronrod quadrature.[47]

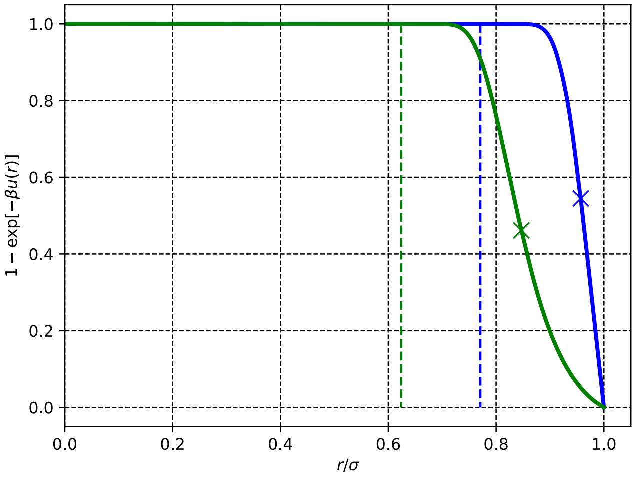

FIG. 2. The integrand of the Barker and Henderson hard-sphere diameter expression [Eq. (59)] for the LJ fluid. The green solid line is for the reduced temperature $T^\star = 30$, and the blue solid line is for $T^\star = 2$. The dashed lines indicate the maximum dimensionless diameter where the integrand numerically equals one on a double-precision computer. The computed hard-sphere diameters are indicated with crosses.

B. Monte Carlo simulations

1. Thermodynamic properties as ensemble averages

To obtain the thermodynamic properties of Mie-FH fluids from simulations, they must be formulated as ensemble averages, denoted as $\langle \cdot \rangle$, in the appropriate ensemble. The procedure is well-known for classical potentials,[48] but the standard formulae for computing residual properties must be modified when the potential depends on temperature. The residual contributions are rigorously derived by taking derivatives of the configurational partition function,

$$\mathcal{Z}(\beta) = \int e^{-\beta V_{\text{FHM}}(\boldsymbol{r}^N;\beta)} \mathrm{d}\boldsymbol{r}^N, \tag{60}$$

where $\boldsymbol{r}^N$ is the vector of positions for N particles and V_{FHM} is the total potential energy of the system. The internal energy per particle is given by

$$\frac{U}{N} = \frac{3}{2} k_{\text{B}} T + \frac{1}{N} \left\langle V_{\text{FHM}}(\boldsymbol{r}^N;\beta) + \beta \frac{\partial V_{\text{FHM}}(\boldsymbol{r}^N;\beta)}{\partial \beta} \right\rangle, \tag{61}$$

where the first term is the ideal gas contribution and the ensemble average is the residual contribution. Equation (61) clearly reduces to the classical formula when the potential is temperature-independent. Equation (61) is equally valid in the NVT, NPT, and μVT ensembles. The isochoric heat capacity is given by

$$\begin{aligned} c_V = {} & \frac{\langle U^2 \rangle_{NVT} - \langle U \rangle_{NVT}^2}{N k_B T^2} \\ & - \frac{1}{N k_B T^2} \left\langle 2 \frac{\partial V_{\text{FHM}}(\boldsymbol{r}^N;\beta)}{\partial \beta} + \beta \frac{\partial^2 V_{\text{FHM}}(\boldsymbol{r}^N;\beta)}{\partial \beta^2} \right\rangle_{NVT}, \end{aligned} \tag{62}$$

with averages in the NVT ensemble as denoted by the subscript. The isobaric heat capacity per particle is given by

$$\begin{aligned} c_P = {} & \frac{\langle H^2 \rangle_{NPT} - \langle H \rangle_{NPT}^2}{N k_B T^2} \\ & - \frac{1}{N k_B T^2} \left\langle 2 \frac{\partial V_{\text{FHM}}(\boldsymbol{r}^N;\beta)}{\partial \beta} + \beta \frac{\partial^2 V_{\text{FHM}}(\boldsymbol{r}^N;\beta)}{\partial \beta^2} \right\rangle_{NPT}, \end{aligned} \tag{63}$$

where $H = U + PV$ is the total enthalpy and the averages are in the NPT ensemble as denoted by the subscript. The expressions for mechanical properties, such as isothermal compressibility, coincide with the classical expressions[48,49] since they do not include temperature derivatives of the partition function.

2. Single-phase NPT simulations

We performed NPT Monte Carlo simulations[48,49] of supercritical Mie-FH fluids to determine densities and isobaric heat capacities. The simulation box contained 750 particles, and we used a cut-off of 4.5σ and the long-range corrections (LRCs) described in the Appendix. Each simulation cycle consisted of, on average, 750 displacement moves and two volume moves. The step lengths for each type of move were adjusted during equilibration toward acceptance ratios between 30% and 50%; the acceptance ratio for displacement will be higher than this for the lowest densities, in which case the step length was set equal to half the box length.

Accurate estimates of heat capacities require long runs. We equilibrated the system for 5×10^4 cycles and then sampled the system for 10^6 cycles. To ensure that our error estimates were within acceptable limits, we ran every *NPT* simulation using two different seeds for the random number generator; the final results are the average of the two runs.

3. Gibbs ensemble Monte Carlo simulations

We performed Gibbs Ensemble Monte Carlo (GEMC) simulations[49,50] of various Mie-FH fluids to determine coexistence properties. A total of 1000 particles were distributed in the vapor and liquid simulation boxes. We applied a (temperature-independent) cutoff of $r_c = 5\sigma$, and during the simulations, we used the long-range corrections described in the Appendix. A Monte Carlo cycle consisted of 1002 moves selected at random that made, on average, 500 displacement attempts, 500 box swap attempts, and 2 volume-change attempts. The maximum volume change and the maximum displacement in each box were adjusted toward an acceptance ratio between 30% and 50%. With these parameters, the simulations seemed to explore the phase space efficiently, yielding reliable estimates for coexistence densities after about 5×10^4 cycles. To increase the accuracy, we equilibrated each simulation with 10^4 cycles and subsequently sampled averages during a production run of 10^6 cycles. Following previous work,[13,51,52] the critical temperature was estimated from the simulations using the renormalization group scaling laws, and the critical pressure was estimated by extrapolating a least-square fit of the Antoine equation $\ln P = A + B/T$.

To ensure a correct GEMC implementation, we verified the equality of pressures and chemical potentials in the two simulation boxes and also verified the phase behavior against independent direct coexistence canonical MD simulations for the Mie(12,6)-FH1 potential.

C. Regression of parameters for real fluids

The number of parameters of the Mie-FH potentials is the same as in Mie potentials, namely, σ, ϵ, λ_a, and λ_r. It has been shown that for the Mie family of fluids, there is a conformality relationship between the exponents λ_a and λ_r, i.e., multiple combinations of (λ_r, λ_a) provide for essentially the same macroscopic properties.[53,54] Hence, it makes sense to employ a fixed value of one of the two exponents while using the second one as an adjustable parameter. Commonly, one will fix $\lambda_a = 6$ consistent with the London dispersion exponent.[53] The final parameter, Λ, is not a fitted parameter but is uniquely determined by the values of σ, ϵ, and the molecular mass. For practical use of the quantum-corrected potentials, these parameters must be determined to represent real fluids with the highest possible accuracy. The influence of quantum effects becomes larger at lower temperatures, where the relative importance depends on the fluid.

In this work, we present parameters for helium, neon, deuterium, and three types of hydrogen; the two spin-isomers *ortho*hydrogen (the protons in the H_2 molecule spin in the same directions), *para*hydrogen (the two protons spin in opposite directions), and *normal*-hydrogen which is a 3-1 mixture of *ortho-para* hydrogen that represents the equilibrium configuration at high temperatures.

We expect the potentials to become less reliable at low enough temperatures, since the Feynman–Hibbs potentials originate in an expansion performed at high temperatures, as discussed in Sec. II A. As SAFT-VRQ Mie does not perfectly predict the thermodynamic properties of Mie-FH fluids, and seeing as a main goal is designing accurate potentials, it is important not to overfit the EoS to properties for which it poorly represents the underlying potential. With this in mind, our procedure for finding the optimal parameters was as follows:

1. We start by identifying the regions and properties where SAFT-VRQ Mie provides the most accurate representation of the underlying potential (see Sec. IV A).
2. We fix $\lambda_a = 6$ and explore $\lambda_r = 8, 9, \ldots, 24$, where for each choice of λ_r, we determine the values of σ and ϵ that minimize the average squared relative deviation between the predictions from SAFT-VRQ Mie and experimental data where it provided a most accurate representation of the underlying potential. The properties used for fitting are saturation pressures and liquid densities, the critical temperature, and supercritical densities and isobaric heat capacities. We used multiparameter EoSs as a substitute for experiments, as these are designed to represent critically evaluated experimental data within their accuracy. We used the EoS by Leachman *et al.*[34] for hydrogen, the EoS by Katti *et al.*[55] for neon, the EoS by Ortiz-Vega[56] for helium, and the EoS by Richardson *et al.*[57] for deuterium.
3. The optimal choice of λ_r was determined both by comparing deviations from experimental data, a visual inspection of both the vapor–liquid equilibrium (VLE) envelope and supercritical isobars, and simulations of the underlying potential to check that they also reproduce the experimental data.

IV. RESULTS AND DISCUSSION

A. The ability of SAFT-VRQ Mie to represent generic Mie-FH fluids

We evaluate the accuracy of SAFT-VRQ Mie in representing the thermodynamic properties of generic Mie potentials with first and second order Feynman–Hibbs corrections (Mie-FH1 and Mie-FH2), by first comparing to results from molecular simulations. Three choices of attractive and repulsive exponents (λ_r, λ_a) will be examined in detail, (10, 6), (12, 6), and (24, 6). These exponents are chosen to span potentials with different degrees of softness. The general trend is that the phase envelopes of Mie-fluids become broader, and the critical temperature and pressure decrease with increasing repulsive exponent. Furthermore, the de Boer parameter has been varied from 1 to 3 to probe a range of quantum corrections. The results for generic Mie fluids have been plotted in terms of reduced variables, namely, reduced temperature $T^\star = k_B T/\epsilon$, reduced pressure $P^\star = P\sigma^3/\epsilon$, reduced number density $\rho^\star = \rho\sigma^3$, and reduced heat capacity per particle $c_p^\star = c_p/k_B$.

Results for the vapor–liquid equilibrium are shown in Fig. 3 for Mie-FH1 and in Fig. 4 for Mie-FH2. Here, the lines are predictions from SAFT-VRQ Mie and the symbols are simulation results from GEMC, including an estimation of the critical point (see Sec. III B 3 for details). Figures 3 and 4 display an excellent agreement between the EoS and the simulation results, both for

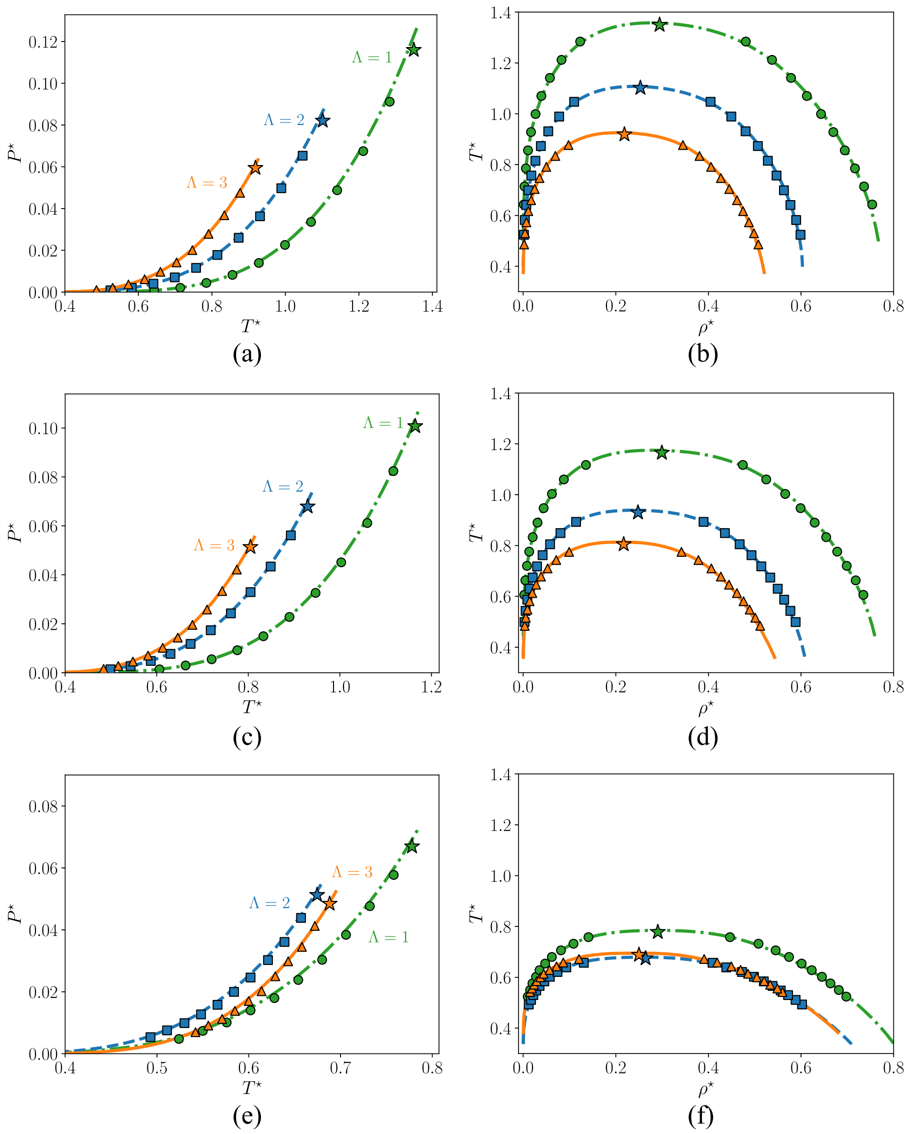

(a) (b)

(c) (d)

(e) (f)

FIG. 3. Vapor–liquid equilibrium diagrams for fluids interacting with Mie-FH1 potentials: Mie(10,6)-FH1 [(a) and (b)], Mie(12,6)-FH1 [(c) and (d)], and Mie(24,6)-FH1 [(e) and (f)]. Symbols are GEMC simulations, while lines are calculations using SAFT-VRQ Mie. Each plot shows three different values of the de Boer parameter: Λ = 1 (dashed-dotted lines, circles), Λ = 2 (dashed lines, squares), and Λ = 3 (solid lines, triangles). The stars are scaling-law estimates of critical points.

saturation densities and pressures, as well as the critical temperature. SAFT-VRQ Mie has a similar accuracy as the present state-of-the-art EoS for classical Mie fluids, which can be seen by comparing the results in Figs. 3 and 4 to the corresponding Figs. 7 and 8 for Mie fluid presented in Ref. 18. This is as good as can be expected, as SAFT-VRQ Mie builds on the developments presented in Ref. 18. Even though the EoS predicts saturation densities to a very high accuracy, the saturation pressures and critical pressure are slightly overestimated. This is particularly visible for the green dashed-dotted lines, where Λ = 1. The same trend can be seen in Fig. 8 of Ref. 18 for classical Mie fluids.

For classical Mie fluids, the critical temperature and pressure decrease when the repulsive exponent λ_r increases with a fixed attractive exponent λ_a.[18,54] The quantum-corrections make the potential shallower and less attractive. Hence, an increase in the de Boer parameter is expected to have a similar effect on the phase envelope as increasing the repulsive exponent of the Mie potential. Figures 3 and 4 show that this is indeed the case for the Feynman–Hibbs-corrected potentials with λ_r = 10 and λ_r = 12. However, λ_r = 24 is an exception from this trend as illustrated in Figs. 3(e), 3(f), 4(e), and 4(f). A comparison of the blue dashed lines and the orange solid lines shows that Λ = 2 gives a higher saturation pressure than Λ = 3 at a given temperature.

The deviation from the trend for λ_r = 24 is caused by the adimensionalization of T, P, and ρ in Figs. 3 and 4, which have been scaled by the parameters of the Mie potentials, ϵ and σ. For Mie-FH1 and Mie-FH2, these parameters differ from ϵ_{eff} and σ_{eff}, and the relative difference becomes larger with increasing repulsive exponent. Figure 1 illustrates that ϵ_{eff} and σ_{eff} are more suitable energy and length scales for the quantum corrected potentials. Indeed, if we use the effective parameters in the scaling, we recover the expected monotonic trend (not shown).

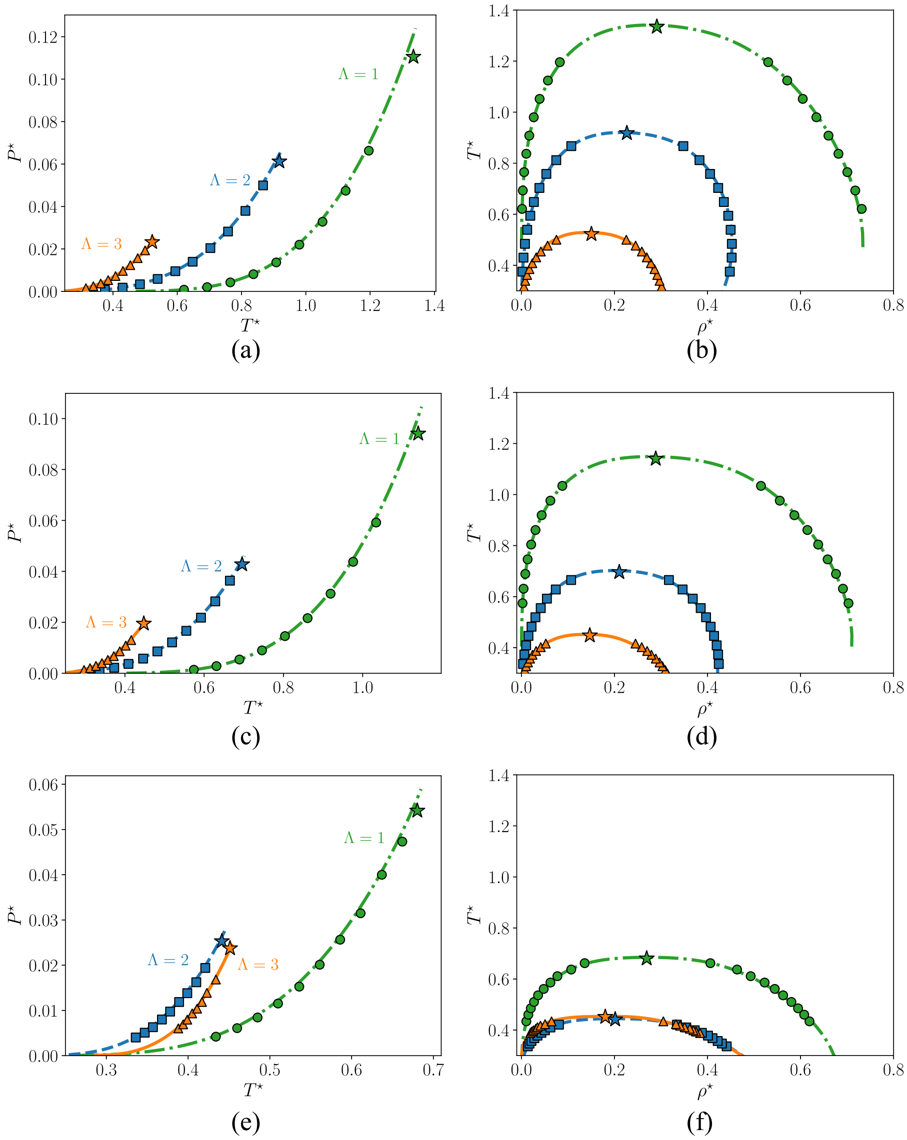

FIG. 4. Vapor–liquid equilibrium diagrams for fluids interacting with Mie-FH2 potentials: Mie(10,6)-FH2 [(a) and (b)], Mie(12,6)-FH2 [(c) and (d)], and Mie(24,6)-FH2 [(e) and (f)]. Symbols are GEMC simulations, while lines are calculations using SAFT-VRQ Mie. Each plot shows three different values of the de Boer parameter: Λ = 1 (dashed-dotted lines, circles), Λ = 2 (dashed lines, squares), and Λ = 3 (solid lines, triangles). The stars are scaling-law estimates of critical points.

Figure 5 shows that SAFT-VRQ Mie also reproduces the supercritical densities and isobaric heat capacities from GEMC simulations to a high accuracy. For supercritical densities, SAFT-VRQ Mie represents the underlying potential nearly within the accuracy of the MC-simulations. Isobaric heat capacities are slightly less accurate, and deviations exceeding 10% can be observed. The softest potential (10,6) with a higher de Boer parameter has the largest relative deviations, which is apparent by comparing the orange triangles with the solid line in Fig. 5(b).

B. Describing real fluids

In Sec. IV A, we established that SAFT-VRQ Mie was capable of describing the thermodynamic properties of generic Mie fluids with Feynman–Hibbs-corrections to a high accuracy. We shall next exploit the one-to-one correspondence between the EoS and the interaction potential to identify the parameters ϵ, σ, λ_a, and λ_r for the Mie-potential (FH0), Mie-FH1, and Mie-FH2 that yield the best possible representation of real fluids. This one-to-one correspondence allows us to use the EoS to fit the model parameters to thermophysical and volumetric properties in a wide range of temperatures, pressures, and densities. While one can then employ the EoS to directly evaluate fluid properties, as an additional benefit, the parameters can also be employed in the molecular simulation of fluids.[60] This is particularly convenient if one wants to study confined fluids.[13]

We have regressed the potential parameters for neon, helium, *ortho*hydrogen, *para*hydrogen, *normal*-hydrogen, and deuterium, and refer to Sec. III C for details on the regression procedure. The parameter λ_a was fixed to the London-dispersion exponent 6, which

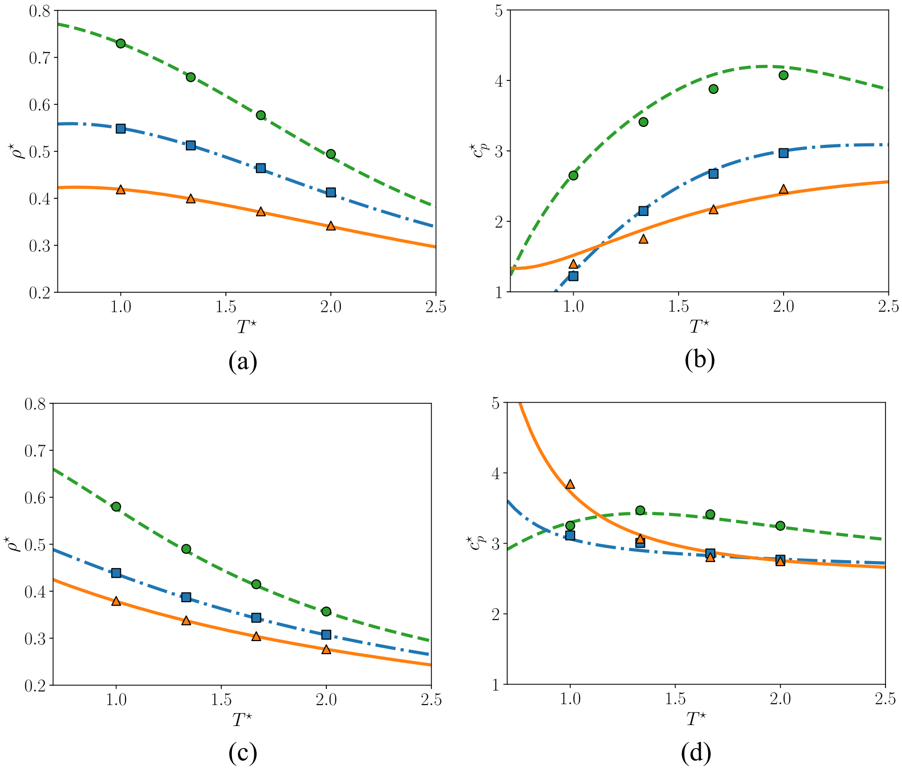

(a)

(b)

(c)

(d)

FIG. 5. Supercritical densities and isobaric heat capacities at reduced pressure $P^* = 1$ for fluids interacting with Mie-FH2 potentials: Mie(10,6)-FH2 [(a) and (b)] and Mie(24,6)-FH2 [(c) and (d)]. Symbols are GEMC simulations, while lines are calculations using SAFT-VRQ Mie. Each plot shows three different values of the de Boer parameter: $\Lambda = 1$ (dashed lines, circles), $\Lambda = 2$ (dashed-dotted lines, squares), and $\Lambda = 3$ (solid lines, triangles).

is the generally recommended choice for modeling fluids with the Mie potential.[59] Other choices for λ_a were investigated, but they did not result in further improvement.

Table II presents the regressed parameters for the interaction potentials of the real fluids and their resultant average absolute relative deviations, commonly referred to as average absolute deviations (AADs), between SAFT-VRQ Mie and the reference EoS. The AADs have been computed both for properties of the VLE envelope (liquid density, pressure, liquid isobaric heat capacity, and critical point) as well as supercritical properties (density, isobaric heat capacity, and speed of sound). The AADs for supercritical properties are averages over four temperatures between 50 K and 300 K, and pressures from 1 bar to 200 bars; helium is an exception in that the lowest temperature used was 20 K.

The general trend for the regressed parameters is that increasing the order of the Feynman–Hibbs correction decreases σ and increases ϵ and λ_r (see Table II). These effects are larger for the fluids that exhibit larger quantum effects, i.e., they are smallest for neon and largest for helium and hydrogen. The trends for ϵ and σ can be rationalized as follows: since these potentials represent the same fluid, their ϵ_{eff} and σ_{eff} should be similar at a given temperature. As discussed in Sec. II A, $\epsilon_{\mathrm{eff}} < \epsilon$ and $\sigma_{\mathrm{eff}} > \sigma$, where the difference increases for higher order quantum correction. The potential parameters in Table II must have the observed trend to counteract this effect.

In the following, we will examine the representation of each fluid in further detail.

1. Neon

To identify the optimal parameters for neon, we used the multiparameter EoS by Katti *et al.*[55] as a reference. For neon, the Feynman–Hibbs quantum corrections do not offer much improvement, as the quantum effects are small. The optimal repulsive exponent was found to be 9.70 for the Mie-fluid,[59] which increases to 13 for Mie-FH1 and Mie-FH2. All three models, Mie-FH0 (no quantum corrections), Mie-FH1, and Mie-FH2 are highly accurate for $PT\rho$-properties. However, Mie-FH0 has a better accuracy for saturation properties, Mie-FH2 yields better supercritical predictions. The Mie-FH1 model gives the most accurate predictions of the isobaric heat capacities of the saturated liquid-phase, where the Mie-FH2 model offers little improvement in comparison to the Mie-fluid. However, this only tells part of the story: the AADs for saturated liquid *isochoric* heat capacity for the Mie-FH0, Mie-FH1, and Mie-FH2 models are 15.03%, 6.43%, and 2.20%, respectively, i.e., a strong, systematic improvement with increasing order of the Feynman–Hibbs correction. This is in agreement with the work by Vlasiuk *et al.*,[61] who also found large improvements for the isochoric heat capacity of neon by employing Feynman–Hibbs-corrections. We note that the reference equation for neon incorporates only a single data set of isochoric heat capacities taken from a 1966 study,[62] so the results should be interpreted with caution.

Figure 6 shows results from SAFT-VRQ Mie for the Mie-FH1 model (dashed lines), the reference EoS for neon (solid lines), simulation results (symbols), and the volume-shifted SRK[63,64]

TABLE II. Optimal parameters for the interaction potentials of real fluids and average absolute deviations (AADs) relative to the reference equations of state.[34,55–57] The properties are saturated liquid density ρ^{sat}, saturation pressure p^{sat}, saturated liquid isobaric heat capacity c_p^{sat}, critical temperature T_c, supercritical density ρ^{sup}, supercritical isobaric heat capacity c_p^{sup}, and supercritical speed of sound w^{sup}.

		Parameters			%AAD						
Substance	FH	σ/Å	(ϵ/k_{B})/K	λ_{r}	ρ^{sat}	p^{sat}	c_p^{sat}	T_c	ρ^{sup}	c_p^{sup}	w^{sup}
D_2	0	3.1538	21.2	8	2.15	5.24	45.15	1.25	1.42	2.19	9.34
D_2	1	3.0203	30.273	10	0.73	0.30	3.18	1.29	0.27	0.59	9.55
D_2	2	2.9897	36.913	12	2.37	4.44	32.44	3.51	0.80	1.24	10.86
H_2	0	3.2574	17.931	8	3.84	9.01	93.32	3.38	3.44	5.76	3.35
H_2	1	3.0243	26.706	9	0.29	2.31	21.59	0.48	0.54	1.84	4.95
H_2	2	2.9195	55.729	20	0.33	2.57	40.09	0.87	0.88	0.48	3.82
He[a]	0	3.3530	4.44	14.84	7.81	56.53	218.99	0.04	16.08	5.78	15.64
He	1	2.7443	5.4195	9	5.48	34.32	177.23	0.84	2.05	2.24	0.87
He	2	2.5490	10.952	13	7.17	38.37	303.24	0.21	0.75	1.90	0.89
Ne[b]	0	2.8019	29.875	9.6977	0.06	0.40	5.98	1.69	0.67	0.82	1.37
Ne	1	2.7778	37.501	13	0.49	0.40	1.39	1.20	0.36	1.16	0.81
Ne	2	2.7760	37.716	13	0.66	0.69	5.17	1.47	0.22	0.91	0.84
O–H_2	0	3.2571	17.935	8	3.82	8.91	93.24	3.58	3.45	5.78	1.24
O–H_2	1	3.0239	26.716	9	0.29	2.22	21.50	0.29	0.52	1.85	1.10
O–H_2	2	2.9191	55.749	20	0.34	2.48	40.08	0.68	0.88	0.56	1.06
P–H_2	0	3.2557	17.849	8	3.91	8.88	91.95	3.22	3.45	5.65	1.30
P–H_2	1	3.0235	26.586	9	0.28	2.22	20.77	0.55	0.50	1.80	1.06
P–H_2	2	2.9185	55.519	20	0.36	2.47	38.70	0.93	0.93	0.44	0.96

[a] Models from Ref. 58.

[b] Models from Ref. 59.

(SRK-VS, dotted line). We evaluated several cubic EoSs and found that the SRK-VS EoS gave the best accuracy for neon. Cubic EoSs such as SRK are known to predict poorly the density of the saturated liquid-phase, and a volume-shift is often used to improve on this.[64]

The agreement of the Mie-FH1 model with both simulations and results from the reference EoS is excellent, and generally much better than SRK. Figures 6(a)–6(e) illustrate that the volume-shift of SRK does not improve the predictions much as it fails to correct the slope of the saturation density line. Table II shows that SAFT-VRQ Mie with Mie-FH1 predicts the saturation density and pressures of neon within a relative accuracy below 0.5%. Similar to in Sec. IV A, SAFT-VRQ Mie agrees with GEMC results to a very high accuracy, with a small deviation at the critical point. The critical temperature and pressure estimated from GEMC are overestimated slightly by SAFT-VRQ Mie, where the Mie-FH1 potential is closer to the experimental results for neon as shown in Fig. 6.

2. Helium

For helium in the supercritical region, quantum corrections vastly improve predictions of the speed of sound, isobaric heat capacity, and density in comparison to the classical Mie-fluid, reducing the AAD in the density and the heat capacity from 16.1% for Mie-FH0 to 2.1% for Mie-FH1 and 0.8% for Mie-FH2, where a higher-order quantum correction gives a more accurate representation.

Figure 7 compares results from SAFT-VRQ Mie with the Mie-FH1 model to the reference EoS by Ortiz-Vega,[56] SRK, and simulation results. It shows that Mie-FH1 is incapable of representing the phase envelope of helium to a high accuracy. The largest deviation is in the saturation pressures of helium, which are significantly underpredicted by the Mie-FH potentials, as shown in Fig. 7(e). This also leads to an underprediction of the vapor-phase densities, as shown in Fig. 7. Similar results were obtained with Mie-FH2.

Of the fluids studied in this work, helium has the largest quantum effects. The fluid phase envelope of helium spans from 2.17 K (triple point) to 5.20 K (critical point). This is much lower than hydrogen, which has the second largest quantum effects and a triple point at 13.8 K. Since the Feynman–Hibbs corrections originate in a high temperature expansion, there is a lower temperature limit where it is no longer expected to be accurate. We find that the Mie-FH1 model represents accurately the thermodynamic properties of the underlying potential and agrees with experiments until about 20 K. This serves as a lower limit for the Feynman–Hibbs-expansion

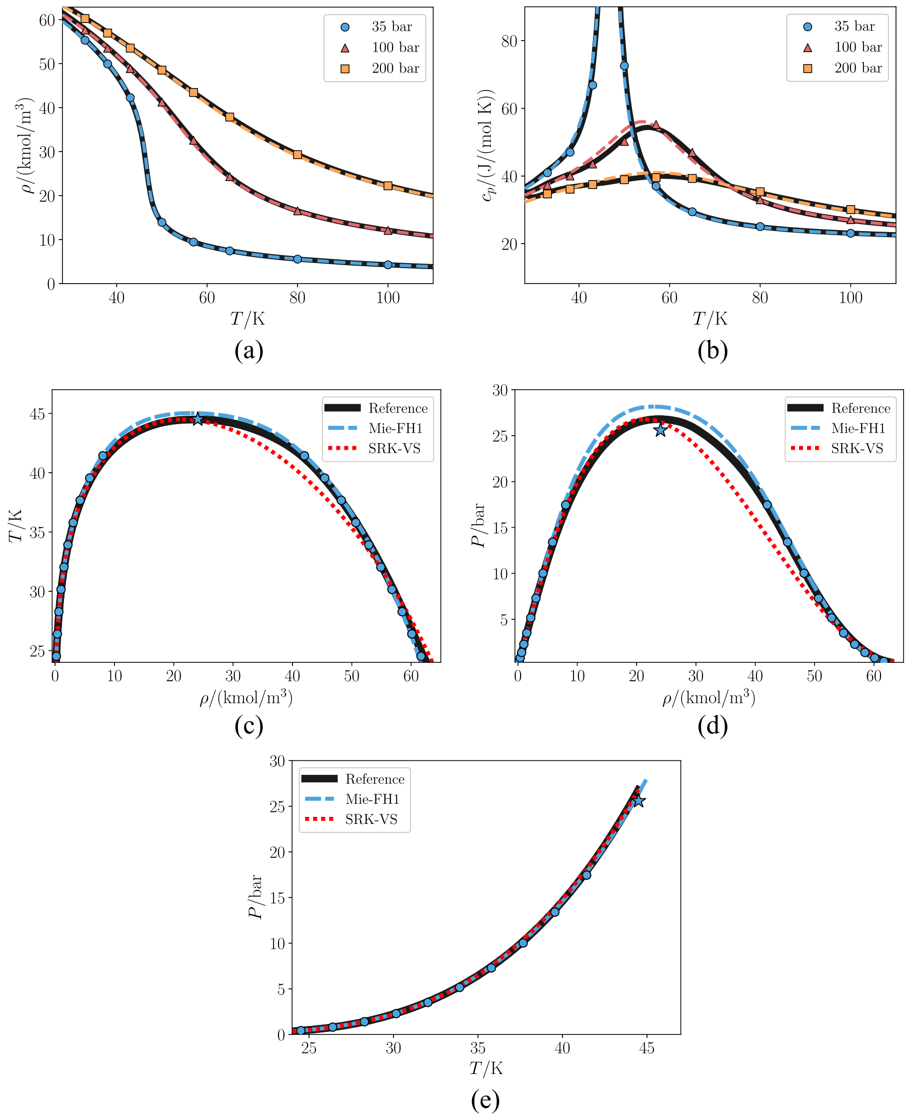

(a) (b) (c) (d) (e)

FIG. 6. Thermodynamic properties of neon: supercritical densities (a), isobaric heat capacities (b), and vapor–liquid equilibrium envelopes [(c)–(e)]. The dashed lines are predictions from SAFT-VRQ Mie for the optimized Mie-FH1 potential and the symbols are the corresponding simulation results, where the stars are scaling-law estimates of the critical point. The solid lines are obtained with the reference EoS for neon,[55] and the dotted lines are obtained with the volume-shifted SRK EoS.[63,64]

for helium. These conclusions are partially supported by the work of Trejos and Gil-Villegas,[24] who developed an EoS for the Feynman–Hibbs-corrected square-well potential. While their EoS yielded good predictions of saturation densities down to 3 K, it severely over-predicted the critical pressure and was inaccurate for supercritical isobaric heat capacities.

The reason for the inadequacy of Feynman–Hibbs corrections may be understood from the low mass and low critical temperature of helium, since the corrections involve powers of the quantity $1/(T\sqrt{m})$. Fortunately, the saturation envelope of helium is at sufficiently low temperatures to be outside the range of most industrial applications, such as hydrogen liquefaction.[14] Only supercritical helium is relevant in this context, and in this region the Feynman–Hibbs-corrected Mie fluids provide an accurate representation of helium at moderate pressures.

3. Orthohydrogen, parahydrogen, and normal-hydrogen

Table II shows how the Feynman–Hibbs corrections significantly improve the representation of both spin-isomers of hydrogen, namely, *ortho*-hydrogen (O–H_2, for which the spins of the protons are the same) and *para*-hydrogen (P–H_2, for which the spins of the protons are opposite), as well as *normal*-hydrogen. *Normal*-hydrogen is synonymous to “hydrogen,” which is the room-temperature equilibrium configuration, consisting of a 3:1 mixture of *ortho* and *para*-hydrogen. In predicting the thermodynamic properties of the hydrogen variants, we find that Mie-FH2 is most accurate at supercritical temperatures, where the AADs of the supercritical density and isobaric heat capacities decrease from 3.4% and 5.8% for the Mie-potential to 0.9% and 0.5% for Mie-FH2. However,

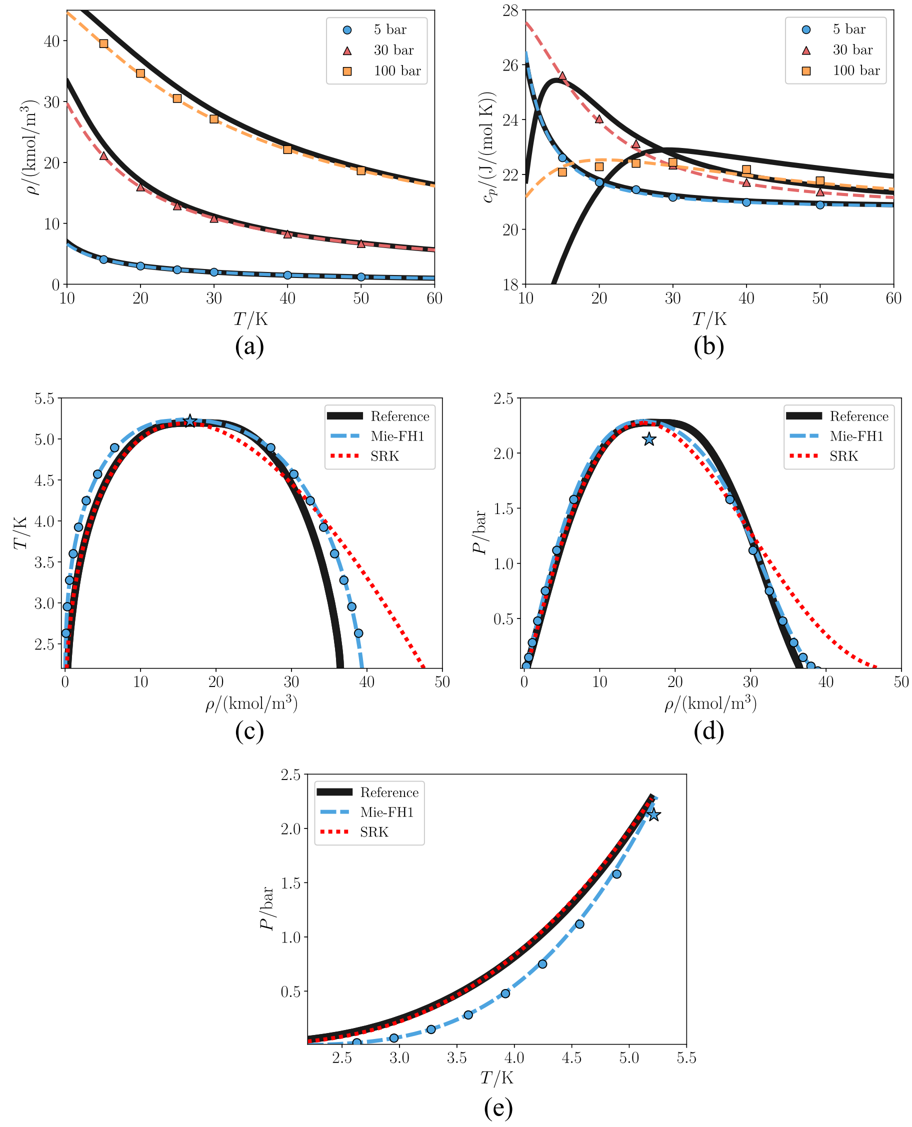

(a) (b) (c) (d) (e)

FIG. 7. Thermodynamic properties of helium: supercritical densities (a), isobaric heat capacities (b), and vapor–liquid equilibrium envelopes [(c)–(e)]. The dashed lines are predictions from SAFT-VRQ Mie for the optimized Mie-FH1 potential, and the symbols are the corresponding simulation results, where the stars are scaling-law estimates of the critical point. The solid lines are obtained with the reference EoS for helium,[56] and the dotted lines are obtained with the SRK EoS.[63]

the Mie-FH1 potential gives the most accurate representation of the VLE region.

The potential parameters for *ortho*- and *para*-hydrogen are different due to the difference in their residual thermodynamic properties, as shown in Tables 13–15 in Ref. 34.

The parameters as well as the AADs of the three types of hydrogen are very similar. This is expected, as the spin properties of the nucleus have a small influence on the effective intermolecular potential, as discussed in Ref. 34. One exception is the speed of sound, w, in the supercritical region, where *ortho* and *para*-hydrogen has significantly lower deviations than *normal*-hydrogen. This makes little sense, as *normal*-hydrogen can be represented accurately as an ideal mixture of its two spin-isomers.[34] A closer inspection of Ref. 34 reveals that no speed-of-sound experiments have been carried out for *normal*-hydrogen in the regions where the AAD was computed. For *para*-hydrogen, where the AAD is lower, there are indeed measurements available,[34] and speed-of-sound data for *ortho*-hydrogen have been manufactured from these by use of the principle of corresponding states.

Figure 8 presents results for the supercritical isobars and the vapor-liquid equilibrium of *normal*-hydrogen in comparison to the highly accurate multiparameter EoS by Leachman *et al.*[34] (solid line). It displays an excellent agreement between SAFT-VRQ Mie and the simulation results (symbols) as well as with the parameterization of the experimental data provided by the multiparameter EoS. SAFT-VRQ Mie improves the predictions by a large margin in comparison to the volume-shifted SRK cubic equation of state (red dotted lines). Similar to neon (see Sec. IV B 1), the GEMC results with the Mie-FH1 potential have a critical pressure which is closer to experiments than SAFT-VRQ Mie.

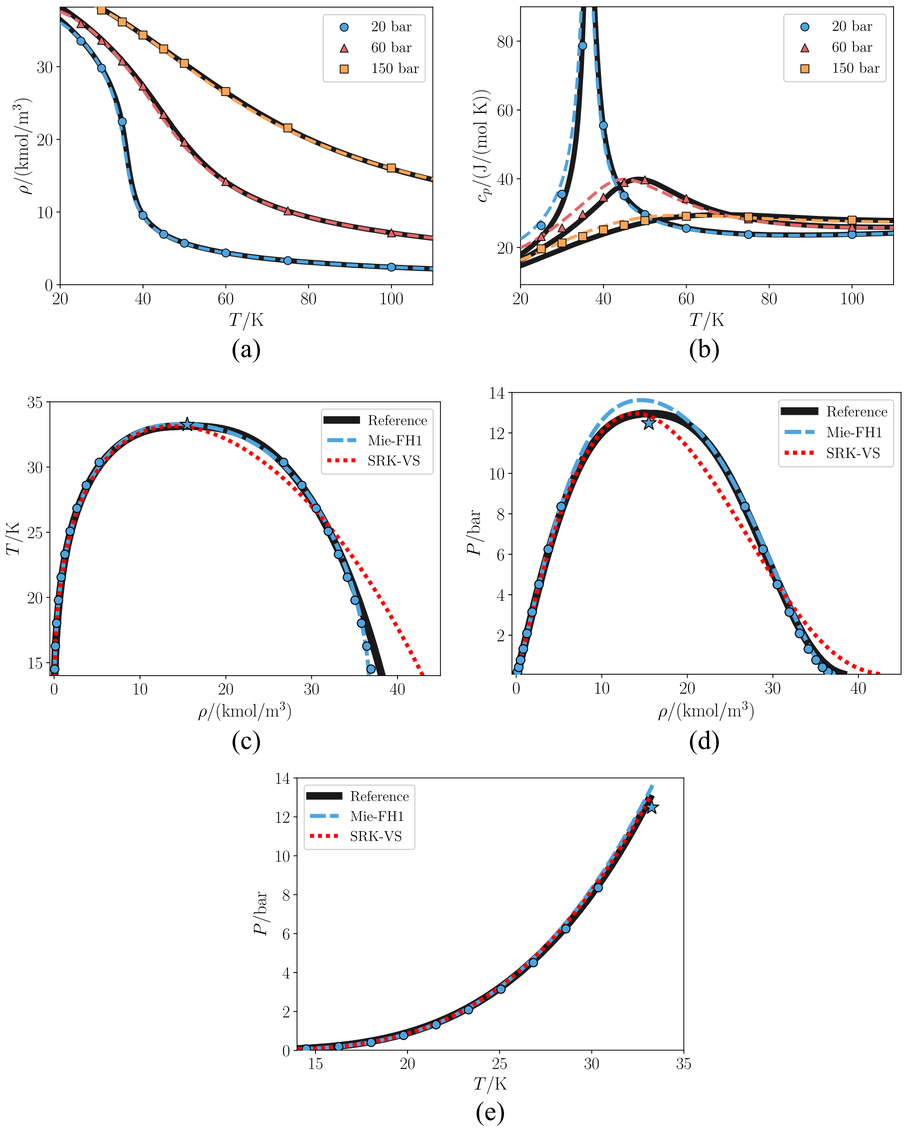

(a) (b) (c) (d) (e)

FIG. 8. Thermodynamic properties of *normal*-hydrogen: supercritical densities (a), isobaric heat capacities (b), and vapor–liquid equilibrium envelopes [(c)–(e)]. The dashed lines are predictions from SAFT-VRQ Mie for the optimized Mie-FH1 potential and the symbols are the corresponding simulation results, where the stars are scaling-law estimates of the critical point. The solid lines are obtained with the reference EoS for *normal*-hydrogen,[34] and the dotted lines are obtained with the volume-shifted SRK EoS.[63,64]

An interesting behavior shown by helium and hydrogen at the phase envelope is that both the specific isobaric and the specific isochoric heat capacities in the saturated vapor are *higher* than that of the corresponding liquid-phase.[34,56] This is also seen to a much smaller extent for deuterium, where the heat capacities are nearly the same in both phases.[57] Classical potentials do not exhibit this feature, but it can be reproduced by the Mie-FH potentials. The formula for the heat capacity of Mie-FH potentials displayed in Eq. (63) has a contribution that includes temperature-derivatives of the potential. Simulations show that this contribution is negative and increases in magnitude with increasing density. By heavily weighing saturation heat capacities in the parameter regression of the Mie-FH potentials, it is possible to qualitatively reproduce this behavior. However, since this will be on the expense of the accuracy of other variables, the specific heat capacities at saturation were not weighed in finding the optimal parameters. With the optimal Mie-FH1 parameters displayed Table II, the heat capacities of the two phases at VLE are almost equal, which gives high AADs of the liquid-phase heat capacities exceed 20%. This is nonetheless an improvement with respect to the Mie-potentials. To ensure that these high AADs are not a result of inaccuracies in the perturbation theory, we performed additional simulations of the Mie-FH1 model for *normal*-hydrogen at saturation densities at 1 bar, which showed excellent agreement with SAFT-VRQ Mie (not shown).

4. Deuterium

We have plotted results for deuterium in Fig. 9. It displays an excellent agreement between SAFT-VRQ Mie with Mie-FH1, simulations and the reference EoS[57] for prediction of phase equilibria as well as supercritical properties.

Similar to hydrogen, deuterium has two spin-isomers, *ortho*- and *para*-deuterium. *Normal* deuterium is a 2:1 mixture of

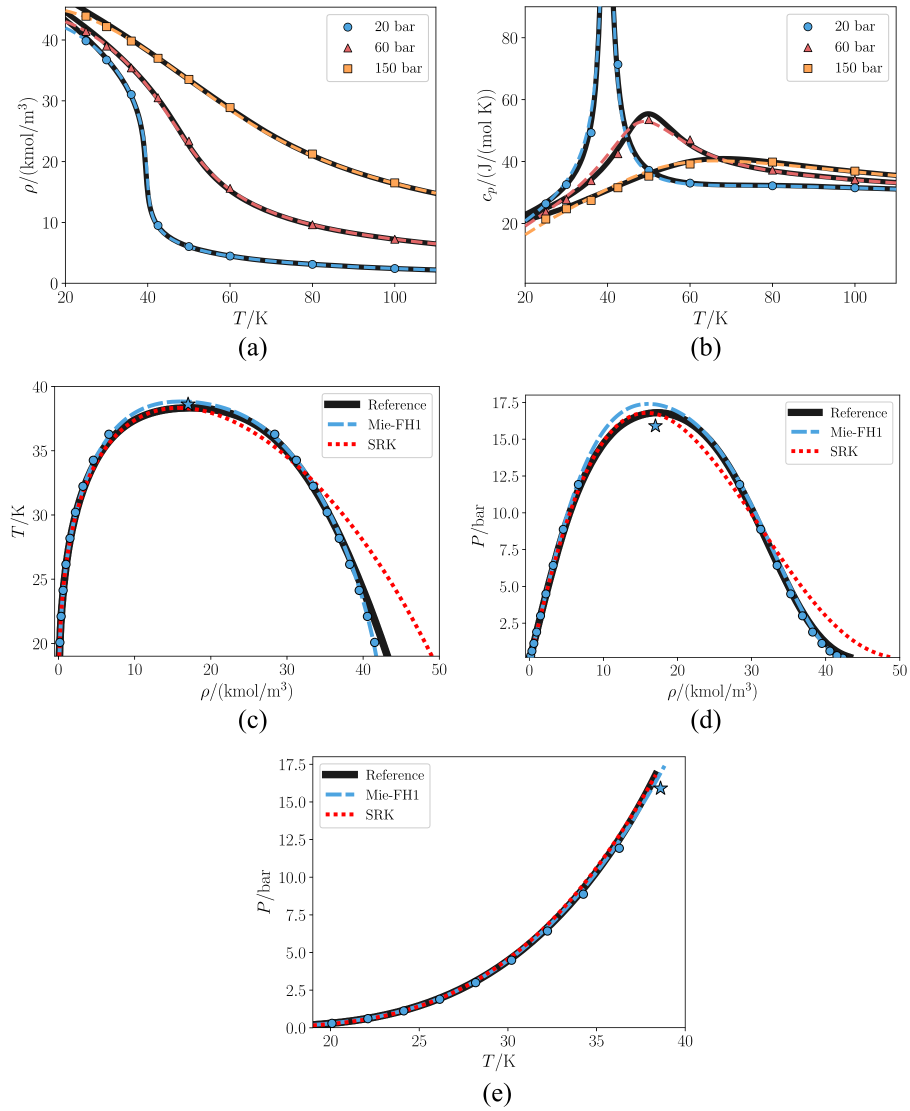

(a)

(b)

(c)

(d)

(e)

FIG. 9. Thermodynamic properties of *normal* deuterium: supercritical densities (a), isobaric heat capacities (b), and vapor–liquid equilibrium envelopes [(c)–(e)]. The dashed lines are predictions from SAFT-VRQ Mie for the optimized Mie-FH1 potential and the symbols are the corresponding simulation results, where the stars are scaling-law estimates of the critical point. The solid lines are obtained with the reference EoS for deuterium,[57] and the dotted lines are obtained with the SRK EoS.[63]

ortho- and *para*-deuterium and is the equilibrium configuration at room temperature.[57] The optimal parameters for *normal* deuterium are shown in Table II. These parameters can also be used to describe residual properties of *ortho*- and *para*-deuterium with SAFT-VRQ Mie. This is justified by the fact that the difference in properties of the spin-isomers of deuterium is smaller than for hydrogen, and the optimal parameters for *normal*-hydrogen are almost equal to those of *ortho*- and *para*-hydrogen (see Table II for details). For caloric properties, one should use the correct ideal gas heat capacities for each spin isomer.[57]

Like helium and hydrogen, deuterium has a lower specific heat capacity in the saturated liquid-phase than in the vapor-phase, even though the difference is smaller than for hydrogen. Only the Mie-FH1 model is capable of reproducing this behavior, where the AAD decreases from 45.2% for Mie-FH0 to 3.5% for Mie-FH1. In fact, the Mie-FH1 model is by far the most accurate for all the properties of deuterium except for the critical temperature and the speed of sound. However, the speed-of-sound measurements for deuterium display a high degree of scatter that may be the cause of some of the deviations between SAFT-VRQ Mie and the reference EoS.[57]

C. General discussion of Feynman–Hibbs corrections

Increasing the order of the Feynman–Hibbs corrections generally yields more accurate results at high temperatures, which is evident from the AADs for most of the fluids in Table II. This is further supported by Fig. 10, which shows an extension of the saturation line into the supercritical TP-space determined by $(\partial c_p/\partial T)_P = 0$, i.e., a maximum of the isobaric heat capacity. The extension shown in Fig. 10 lies close to what is called the Widom line.[65] It forms a continuous extension of the saturation line and goes through a region of abrupt (but continuous) change in density, as illustrated

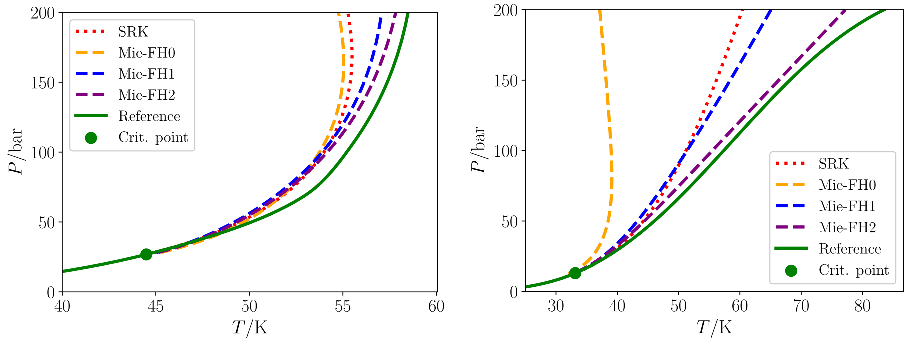

(a) (b)

FIG. 10. The experimental critical point (green circle) and locus corresponding to $\left(\partial c_p/\partial T\right)_P = 0$ for the components neon (a) and hydrogen (b) using SAFT-VRQ Mie with optimized parameters (dashed lines) and the SRK EoS[63] (dotted lines). The green solid line is computed from the reference EoS,[34,55] where the states below the critical point are saturation points.

in, e.g., Fig. 8(a). For all real fluids we consider in this paper, increasing the Feynman–Hibbs-order of the model yields more accurate predictions of this line.

Although SAFT-VRQ Mie gives a highly accurate representation of the thermodynamic properties of Mie-FH1 and Mie-FH2 fluids, we find that the simulated properties of the molecular models often lie closer to experimental data than the perturbation theory. An example is hydrogen, where Fig. 8 shows that the simulations are usually closer to the reference data than the predictions by SAFT-VRQ Mie. This indicates that there is a potential for further improving the perturbation theory, in particular near the critical point. Moreover, this also shows that we have avoided overfitting the EoS to regions where the underlying perturbation theory is inaccurate in determining the optimal fluid parameters.

Furthermore, the force field implicit in the parameter fitting shows to be robust and transferable and is appropriate for large molecular simulations (either in size or complexity) to probe confinement, transport properties, etc. This is a well-established approach for classical Mie fluids.[66–68]

Previous work[13] has suggested that the LJ-FH1 potential yields an accurate representation of the VLE envelope of neon, normal hydrogen, and helium. By performing GEMC simulations with the same potentials, we were able to reproduce their simulation results for neon and hydrogen, but obtained different results for helium. Since SAFT-VRQ Mie accurately reproduces all the new GEMC results (not shown), we believe the GEMC data presented for helium in Ref. 13 to be incorrect.

Finally, we mention that supercritical densities and heat capacities for real fluids are more accurately predicted by SAFT-VRQ Mie than the SRK EoS. This is not shown in Figs. 6–9 to ease readability.

V. CONCLUSION

Classical interaction potentials with Feynman–Hibbs corrections can be used to accurately describe the thermophysical properties of fluids influenced by quantum effects at low temperatures such as helium, hydrogen, neon, and deuterium. In this work, we have presented an equation of state (EoS) for Mie-fluids with first (Mie-FH1) and second-order Feynman–Hibbs corrections (Mie-FH2). The EoS is based on perturbation theory with a third-order Barker–Henderson expansion of the Helmholtz energy. The EoS is called SAFT-VRQ Mie, where Q is short for quantum. This paper is the first in a series of two, where Paper II will be devoted to mixtures.[69]

We demonstrated that the SAFT-VRQ Mie EoS reproduces accurately results from Monte Carlo simulations for generic Mie-FH1 and Mie-FH2 fluids, where it displays a similar accuracy as the present state-of-the-art for classical Mie fluids. We next exploited the link between the EoS and the interaction potentials to find the optimal force-field parameters to represent the thermodynamic properties of neon, helium, *normal*-hydrogen, *ortho*-hydrogen, *para*-hydrogen, and deuterium. Highly accurate multiparameter EoSs that represent most available experimental data within their accuracy were used as references.

For all examined fluids, the Feynman–Hibbs corrections significantly improved the accuracy in the supercritical regions, where Mie-FH2 was slightly more accurate than Mie-FH1 except for deuterium. The improvement in absolute average deviation (AAD) for supercritical properties was largest for the fluids with the highest de Boer parameters, hydrogen and helium, where the AADs of supercritical densities were reduced from 16% and 3.4% for the Mie-fluids to 0.8% for Mie-FH2. The Mie-FH1 potential was found to give the most accurate representation of the phase envelopes for all fluids except helium. Only a modest improvement at high temperatures was obtained by increasing the order of the quantum corrections from one to two, and Mie-FH2 extrapolated more poorly to low temperatures than Mie-FH1.

We found that both Mie-FH1 and Mie-FH2 underpredict the saturation pressure of helium, which results in an underprediction of the densities of the saturated vapor-phase. We presume that this corresponds to a break-down of the high-temperature expansion, and its validity for helium starts to become questionable at temperatures below 20 K. Unlike classical fluids, helium and hydrogen have specific isobaric heat capacities for the saturated vapor-phase which are higher than those of the liquid-phase. The optimal parameters for Mie-FH1 and Mie-FH2 do not reproduce this behavior qualitatively, and the isobaric heat capacities of these fluids are poorly represented for the saturated liquid-phase.

The potentials developed in the present work are sufficiently accurate for a wide range of applications. To further increase the accuracy or extend the range of applicability of the semiclassical potential approach, we expect that using a more general functional form than Mie potentials will yield little improvement. Instead, perturbing from a quantum hard-sphere system is a promising path toward further refining the semiclassical potential modeling approach.

ACKNOWLEDGMENTS

The authors thank Alejandro Gil-Villegas, George Jackson, Amparo Galindo, and Sondre Schnell for illuminating discussions. Ailo Aasen and Øivind Wilhelmsen were supported by the ENERSENSE initiative for which they are grateful. Ailo Aasen, Morten Hammer, Åsmund Ervik, and Øivind Wilhelmsen were supported by the HYVA project, which is part of the Strategic Institute Programme of SINTEF Energy Research funded through the Basic Research Funding scheme of the Research Council of Norway. Erich A. Müller was supported by the Engineering and Physical Sciences Research Council (EPSRC) of the UK through Grant Nos. EP/EP016340, EP/J014958, and EP/R013152 to the Molecular Systems Engineering Group.

APPENDIX: LONG-RANGE CORRECTIONS TO THE PRESSURE AND ENERGY FOR THE MIE-FH POTENTIAL

When performing computer simulations of the Mie potential with Feynman–Hibbs corrections, the potential is usually truncated at a certain cutoff radius r_c. To correct for this, one introduces long-range corrections (LRCs). The Mie-FH2 potential can be written as $u(r, \beta) = u_C(r) + u_D(r, \beta) + u_{DD}(r, \beta)$, where u_C is the Mie potential, u_D is the FH1 correction, and $u_D + u_{DD}$ is the FH2 correction. Since the LRCs are additive, it suffices to give the long-range corrections for u_C, u_D, and u_{DD} separately; for example, the long-range correction to the energy per particle can be split as $E^{\mathrm{LRC}} = E_{\mathrm{C}}^{\mathrm{LRC}} + E_D^{\mathrm{LRC}} + E_{DD}^{\mathrm{LRC}}$. The corrections to the pressure and energy are given by the general formulae $P^{\mathrm{LRC}} = -(2\pi\rho^2/3)\int_{r_c}^{\infty}\frac{\mathrm{d}u}{\mathrm{d}r}r^3\mathrm{d}r$ and $E^{\mathrm{LRC}} = (\rho/2)\int_{r_c}^{\infty}4\pi r^2 u(r)\mathrm{d}r$, which means that

$$E_{\mathrm{C}}^{\mathrm{LRC}} = 2\pi\rho\mathcal{C}\epsilon\left[\frac{\sigma^{\lambda_r}}{(\lambda_r-3)r_c^{\lambda_r-3}} - \frac{\sigma^{\lambda_a}}{(\lambda_a-3)r_c^{\lambda_a-3}}\right], \tag{A1}$$

$$E_D^{\mathrm{LRC}} = 2\pi\rho\mathcal{C}\epsilon D\left[\frac{\lambda_r\sigma^{\lambda_r}}{r_c^{\lambda_r-1}} - \frac{\lambda_a\sigma^{\lambda_a}}{r_c^{\lambda_a-1}}\right], \tag{A2}$$

$$E_{DD}^{\mathrm{LRC}} = \pi\rho\mathcal{C}\epsilon D^2\left[\frac{(\lambda_r+2)\lambda_r(\lambda_r-1)\sigma^{\lambda_r}}{r_c^{\lambda_r+1}} - \frac{(\lambda_a+2)\lambda_a(\lambda_a-1)\sigma^{\lambda_a}}{r_c^{\lambda_a+1}}\right], \tag{A3}$$

$$P_{\mathrm{C}}^{\mathrm{LRC}} = \frac{2\pi\rho^2\mathcal{C}\epsilon}{3}\left[\frac{\lambda_r\sigma^{\lambda_r}}{(\lambda_r-3)r_c^{\lambda_r-3}} - \frac{\lambda_a\sigma^{\lambda_a}}{(\lambda_a-3)r_c^{\lambda_a-3}}\right], \tag{A4}$$

$$P_D^{\mathrm{LRC}} = \frac{2\pi\rho^2\mathcal{C}\epsilon}{3}D\left[\frac{\lambda_r(\lambda_r+2)\sigma^{\lambda_r}}{r_c^{\lambda_r-1}} - \frac{\lambda_a(\lambda_a+2)\sigma^{\lambda_a}}{r_c^{\lambda_a-1}}\right], \tag{A5}$$

$$P_{DD}^{\mathrm{LRC}} = \frac{\pi\rho^2\mathcal{C}\epsilon}{3}D^2\left[\frac{(\lambda_r+4)(\lambda_r+2)\lambda_r(\lambda_r-1)\sigma^{\lambda_r}}{r_c^{\lambda_r+1}} - \frac{(\lambda_a+4)(\lambda_a+2)\lambda_a(\lambda_a-1)\sigma^{\lambda_a}}{r_c^{\lambda_a+1}}\right]. \tag{A6}$$

REFERENCES

[1] E. Wigner, Phys. Rev. **40**, 749 (1932).

[2] J. G. Kirkwood, Phys. Rev. **44**, 31 (1933).

[3] R. P. Feynman, A. R. Hibbs, and D. F. Styer, *Quantum Mechanics and Path Integrals*, Emended ed. (McGraw-Hill, New York, 2005), p. 384.

[4] S. Kim, D. Henderson, and J. Barker, Can. J. Phys. **47**, 99 (1969).

[5] C. Gray and K. Gubbins, *Theory of Molecular Fluids: Volume 1: Fundamentals* (Oxford University Press, 1984).

[6] K. Lucas, *Applied Statistical Thermodynamics* (Springer-Verlag, 1991).

[7] D. A. McQuarrie, *Statistical Mechanics* (Harper & Row, New York, 1976).

[8] A. V. A. Kumar, H. Jobic, and S. K. Bhatia, J. Phys. Chem. B **110**, 16666 (2006).

[9] J. M. Salazar, S. Lectez, C. Gauvin, M. Macaud, J. P. Bellat, G. Weber, I. Bezverkhyy, and J. M. Simon, Int. J. Hydrogen Energy **42**, 13099 (2017).

[10] F. Calvo, J. P. K. Doye, and D. J. Wales, J. Chem. Phys. **114**, 7312 (2001).

[11] R. Rodríguez-Cantano, R. Pérez de Tudela, M. Bartolomei, M. I. Hernández, J. Campos-Martínez, T. González-Lezana, P. Villarreal, J. Hernández-Rojas, and J. Bretón, J. Phys. Chem. A **120**, 5370 (2016).

[12] P. Kowalczyk, L. Brualla, P. Gauden, and A. P. Terzyk, Phys. Chem. Chem. Phys. **11**, 9182 (2009).

[13] V. M. Trejos, A. Gil-Villegas, and A. Martinez, J. Chem. Phys. **139**, 184505 (2013).

[14] Ø. Wilhelmsen, D. Berstad, A. Aasen, P. Nekså, and G. Skaugen, Int. J. Hydrogen Energy **43**, 5033 (2018).

[15] R. Span, *Multiparameter Equations of State* (Springer-Verlag, Berlin, 2000).

[16] Ø. Wilhelmsen, A. Aasen, G. Skaugen, P. Aursand, A. Austegard, E. Aursand, M. A. Gjennestad, H. Lund, G. Linga, and M. Hammer, Ind. Eng. Chem. Res. **56**, 3503 (2017).

[17] P. J. Leonard, D. Henderson, and J. A. Barker, Trans. Faraday Soc. **66**, 2439 (1970).

[18] T. Lafitte, A. Apostolakou, C. Avendaño, A. Galindo, C. S. Adjiman, E. A. Müller, and G. Jackson, J. Chem. Phys. **139**, 154504 (2013).

[19] Ø. Wilhelmsen, T. T. Trinh, A. Lervik, V. K. Badam, S. Kjelstrup, and D. Bedeaux, Phys. Rev. E **93**, 032801 (2016).

[20] D. M. Ceperley, Rev. Mod. Phys. **67**, 279 (1995).

[21] Q. Wang and J. K. Johnson, Fluid Phase Equilib. **132**, 93 (1997).

[22] L. M. Sesé and R. Ledesma, J. Chem. Phys. **102**, 3776 (1995).

[23] L. M. Sesé and L. E. Bailey, J. Chem. Phys. **119**, 10256 (2003).

[24] V. M. Trejos and A. Gil-Villegas, J. Chem. Phys. **136**, 184506 (2012).

[25] B. Singh and S. Sinha, J. Chem. Phys. **67**, 3645 (1977).

[26] B. Singh and S. Sinha, J. Chem. Phys. **68**, 562 (1978).

[27] S. Contreras, C. Serna, and A. Gil-Villegas, Mol. Phys. **116**, 3425–3433 (2018).

[28] A. Gil-Villegas, A. Galindo, P. J. Whitehead, S. J. Mills, G. Jackson, and A. N. Burgess, J. Chem. Phys. **106**, 4168 (1997).

[29] V. Papaioannou, T. Lafitte, C. Avendaño, C. S. Adjiman, G. Jackson, E. A. Müller, and A. Galindo, J. Chem. Phys. **140**, 054107 (2014).

[30] C. Serna and A. Gil-Villegas, Mol. Phys. **114**, 2700 (2016).

[31] C. Bender and S. Orszag, *Advanced Mathematical Methods for Scientists and Engineers* (Springer, New York, 2005).

[32] J.-P. Hansen and J.-J. Weis, Phys. Rev. **188**, 314 (1969).

[33] L. M. Sesé, Mol. Phys. **85**, 931 (1995).

[34] J. W. Leachman, R. T. Jacobsen, S. G. Penoncello, and E. W. Lemmon, J. Phys. Chem. Ref. Data **38**, 721 (2009).

[35] J. K. Jaen and A. A. Khan, J. Chem. Phys. **46**, 260 (1967).

[36] H. S. Green, J. Chem. Phys. **19**, 955 (1951).

[37] J. A. Barker and D. Henderson, J. Chem. Phys. **47**, 4714 (1967).

[38] N. F. Carnahan and K. E. Starling, J. Chem. Phys. **51**, 635 (1969).

[39] J. A. Barker and D. Henderson, Rev. Mod. Phys. **48**, 587 (1976).

[40] C. Avendaño, T. Lafitte, C. S. Adjiman, A. Galindo, E. A. Müller, and G. Jackson, J. Phys. Chem. B **117**, 2717 (2013).

[41] I. Nezbeda and G. A. Iglesias-Silva, Mol. Phys. **69**, 767 (1990).

[42] M. S. Wertheim, J. Math. Phys. **8**, 927 (1967).

[43] Ø. Wilhelmsen, G. Skaugen, M. Hammer, P. E. Wahl, and J. C. Morud, Ind. Eng. Chem. Res. **52**, 2130 (2013).
[44] A. Aasen, M. Hammer, G. Skaugen, J. Jakobsen, and Ø. Wilhelmsen, Fluid Phase Equilib. **442**, 125 (2017).
[45] M. L. Michelsen and J. M. Mollerup, *Thermodynamic Models: Fundamentals & Computational Aspects* (Tie-Line Publications, Holte, 2007).
[46] P. Aursand, M. A. Gjennestad, E. Aursand, M. Hammer, and Ø. Wilhelmsen, Fluid Phase Equilib. **436**, 98 (2017).
[47] D. Kahaner, C. Moler, and S. Nash, *Numerical Methods and Software* (Prentice-Hall, New Jersey, 1989).
[48] D. Frenkel and B. Smit, *Understanding Molecular Simulation: From Algorithms to Applications*, 2nd ed. (Academic Press, New York, 2002).
[49] M. Allen and D. Tildesley, *Computer Simulation of Liquids*, 2nd ed. (Oxford University Press, New York, 2017).
[50] A. Z. Panagiotopoulos, Mol. Phys. **61**, 813 (1987).
[51] J. Rowlinson and B. Widom, *Molecular Theory of Capillarity* (Clarendon Press, Oxford, 1984).
[52] L. Vega, E. de Miguel, L. F. Rull, G. Jackson, and I. A. McLure, J. Chem. Phys. **96**, 2296 (1992).
[53] A. Mejía, C. Herdes, and E. A. Müler, Ind. Eng. Chem. Res. **53**, 4131 (2014).
[54] N. Ramrattan, C. Avendaño, E. Müller, and A. Galindo, Mol. Phys. **113**, 932 (2015).
[55] R. Katti, R. Jacobsen, R. Stewart, and M. Jahangiri, Adv. Cryog. Eng. **31**, 1189 (1986).
[56] D. O. Ortiz-Vega, "A new wide range equation of state for helium-4," Ph.D. thesis, Texas A&M University, 2013.
[57] I. A. Richardson, J. W. Leachman, and E. W. Lemmon, J. Phys. Chem. Ref. Data **43**, 013103 (2014).
[58] C. Herdes, T. S. Totton, and E. A. Müller, Fluid Phase Equilib. **406**, 91 (2015).
[59] S. Dufal, T. Lafitte, A. Galindo, G. Jackson, and A. J. Haslam, AIChE J. **61**, 2891 (2015).
[60] E. A. Müller and G. Jackson, Annu. Rev. Chem. Biomol. Eng. **5**, 405 (2014).
[61] M. Vlasiuk, F. Frascoli, and R. J. Sadus, J. Chem. Phys. **145**, 104501 (2016).
[62] C. Gladun, Cryogenics **6**, 27 (1966).
[63] G. Soave, Chem. Eng. Sci. **27**, 1197 (1972).
[64] A. Péneloux, E. Rauzy, and R. Fréze, Fluid Phase Equilib. **8**, 7 (1982).
[65] M. Raju, D. T. Banuti, P. C. Ma, and M. Ihme, Sci. Rep. **7**, 3027 (2017).
[66] G. Jiménez-Serratos, C. Herdes, A. J. Haslam, G. Jackson, and E. A. Müller, Macromolecules **50**, 4840 (2017).
[67] F. Jaeger, O. K. Matar, and E. A. Müller, J. Chem. Phys. **148**, 174504 (2018).
[68] S. Shahruddin, G. Jiménez-Serratos, G. Britovsek, O. Matar, and E. A. Müller, Sci. Rep. **9**, 1002 (2019).
[69] A. Aasen, M. Hammer, Å. Ervik, E. A. Müller, and Ø. Wilhelmsen, "Equation of state and force fields for Feynman-Hibbs-corrected Mie fluids. II. Application to mixtures of helium, neon, hydrogen and deuterium" (unpublished).